International Journal of Heat and Mass Transfer 236 (2025) 126314

Contents lists available at ScienceDirect

International Journal of Heat and Mass Transfer

journal homepage: www.elsevier.com/locate/hmt

Direct numerical simulations of centrifugal convection: From gravitational to centrifugal buoyancy dominance

Zhongzhi Yao, Mohammad S. Emran, Andrei Teimurazov, Olga Shishkina *

Max Planck Institute for Dynamics and Self-Organization, Am Fassberg 17, Göttingen, 37077, Germany

ARTICLE INFO

Keywords:
Thermal convection
Centrifugal convection
Rayleigh–Bénard convection
Vertical convection
Natural convection
Rotating convection
Direct numerical simulations
Turbulence

ABSTRACT

We report the results of direct numerical simulations (DNS) of centrifugal convection (CC) in an annular container, heated at the outer sidewall and cooled at the inner wall, all subjected to a constant rotation around the vertical axis. This setup mimics the annular centrifugal Rayleigh–Bénard convection (ACRBC) facility used in the CC experiments in Chao Sun's Lab at Tsinghua University. For a fixed size of the container and a given fluid, the strengths of centrifugal and thermal driving in such a system are characterized, respectively, by the dimensionless Froude number Fr and Rayleigh number Ra. Our DNS of CC cover the following range of control parameters: $0 \le Fr \le 100$ and $2\times10^5 \le Ra \le 8.88\times10^8$. For a fixed Ra, with increasing Fr from 0 (no-rotation) to 100 (strong centrifugal buoyancy), we observe an evolution of the global flow structure and heat transport scaling properties from those typical for vertical convection, where the imposed temperature gradient is orthogonal to the driving force (gravitational buoyancy), to those typical for Rayleigh–Bénard convection, where the temperature gradient is parallel to the force (centrifugal buoyancy). With increasing centrifugal buoyancy, the flow undergoes a transition from a three-dimensional global flow structure to a quasi-two-dimensional one, which is characterized by a suppressed mixing in the vertical direction (Taylor–Proudman theorem). Our DNS show that for larger values of Ra, larger Fr values are required for the transition.

1. Introduction

Thermally driven turbulent flows are ubiquitous in astrophysical and geophysical systems and are important in various engineering applications [1–3]. The paradigmatic systems for investigating such natural convection system are Rayleigh–Bénard convection [4–11], where a fluid is confined between a warmer lower surface and a cooler upper surface, horizontal convection, see e.g. [12–19], driven by differential heating and cooling across distinct regions of the same, top or bottom, horizontal surface of the fluid layer, and vertical convection, see, e.g., [20–26], occurring between two unequally heated isothermal vertical surfaces.

The main non-dimensional control parameter in all these natural convection systems is the Rayleigh number $Ra \equiv \alpha g_z L^3 \Delta/(\kappa\nu)$, where α is the thermal expansion coefficient, g_z the acceleration due to gravity, L the distance between the differently heated surfaces of the container, Δ the maximal temperature difference at the container surfaces, ν the kinematic viscosity of the working fluid, and κ the thermal diffusivity. Next to Ra, also the Prandtl number $Pr \equiv \nu/\kappa$ (a fluid property) and the container aspect ratios (geometrical characteristics of the container) are control parameters of the system.

The most relevant to complex geophysical and astrophysical flows is the regime of extremely large Rayleigh numbers [11,27]. One can achieve this regime by increasing the temperature difference Δ or the distance between the heated and cooled surfaces L [see, e.g., 28–30], or by optimizing the fluid properties, usually by decreasing the kinematic viscosity ν and/or thermal diffusivity κ [see, e.g., 31,32]. Finally, one can increase the driving acceleration in the system. In terrestrial experiments, it is impossible to change the gravitational acceleration g_z in the standard natural convection setups mentioned above, however, it is possible to achieve high centrifugal accelerations in centrifugal facilities.

Such a novel facility – the annular centrifugal Rayleigh–Bénard convection (ACRBC) facility – was built at Tsinghua University, in Chao Sun's Lab, and the experiments for the centrifugal accelerations up to 100 times larger than the gravitational acceleration g_z were conducted [33,34]. In these experiments of centrifugal convection (CC) by very fast rotation, the effect of the gravitational acceleration can be considered as negligible compared to the centrifugal acceleration, therefore the convective processes in the ACRBC experiments are similar to those in classical Rayleigh–Bénard convection. This opens the possibility to study experimentally the scaling relations for the heat

* Corresponding author.
E-mail address: olga.shishkina@ds.mpg.de (O. Shishkina).

https://doi.org/10.1016/j.ijheatmasstransfer.2024.126314
Received 6 August 2024; Received in revised form 6 September 2024; Accepted 9 October 2024
Available online 24 October 2024

and momentum transport versus the control parameters in Rayleigh–Bénard convection, in particular, for extremely large Rayleigh numbers associated with the so-called ultimate regime of thermal convection, see Lohse and Shishkina [11,27] and Roche [32].

A general CC flow configuration resembles a combination of Rayleigh–Bénard convection for extremely rapid rotation and vertical convection for no rotation. Thus, the concept of CC is close to the concept of inclined convection, which is a generalization of Rayleigh–Bénard convection and vertical convection, and where the fluid layer between the parallel and differently heated plates is tilted with respect to the direction of gravity, so that both, buoyancy and shear affect the fluid flow. Inclined turbulent convection has been relatively actively studied experimentally, see, e.g., [35–46], and there are also a few numerical studies, see [47–51].

Another flow configuration, which is also closely related to the CC and inclined convection systems, is a setup where the differential heating and cooling of two vertical walls (like in vertical convection) is combined with the differential heating and cooling of the two horizontal, top and bottom, plates (like in Rayleigh–Bénard convection). Such flow configuration has been studied much less than inclined convection, however, some experimental and numerical studies exist, see [52–54].

In this paper, we report the results of direct numerical simulations (DNS) of centrifugal convection (CC) in a setup that mimics the ACRBC facility [33,34]. However, in our study we also consider the cases of relatively weak rotation but considerable thermal driving, where the effect of the gravitational acceleration is non-negligible and can be even dominating. In contrast to the simulations from [33,34] (which were conducted in addition to the main experimental study in that work), we consider realistic top and bottom boundary conditions, in accordance with the experimental ones, and always take into account the gravitational acceleration. To make our simulations feasible over a broad range of the parameters Ra and Fr, in most of our simulations we keep small the size of our virtual container, with the outer annulus radius of $R = 6$ cm. However, in addition, to make a connection to the experiments in the ACRBC facility, we conduct two simulations for $R = 24$ cm, as in the ACRBC experiments.

2. Centrifugal convection setup and its dimensionless control parameters

In the setup we consider a vertically aligned cylindrical annulus (same as in the experiments [33,34]) with top and bottom solid walls, featuring a cooled inner sidewall and a heated outer sidewall, all subject to a constant rotation around the vertical axis of the annulus is employed, see a schematic diagram of the centrifugal convection (CC) setup in Fig. 1.

More precisely, the annular container with a height H, an outer radius R, and a gap L between the inner and outer vertical walls (coloured blue and pink in Fig. 1, respectively) is rotated clockwise around the annulus's vertical axis[1] at a constant angular velocity $\Omega \geq 0$. The outer vertical wall is maintained at a temperature θ_+, and the inner vertical wall is kept at a temperature θ_-, so that $\Delta \equiv \theta_+ - \theta_- > 0$. The horizontal top and bottom walls are perfectly insulated, adhering to the adiabatic thermal boundary conditions. The velocity vanishes at all horizontal and vertical walls of the container, $\boldsymbol{u} = 0$, reflecting the no-slip boundary conditions, see Fig. 1.

A CC container, which is bounded by the annulus vertical solid walls separated by a distance L and the top and bottom horizontal solid walls separated by the height H, is characterized by the following geometrical dimensionless control parameters of the CC system:

$$\Gamma_\phi \equiv 2\pi R/L \quad \text{and} \quad \Gamma_H \equiv H/L, \tag{1}$$

which can be interpreted as the aspect ratios of the container in the azimuthal and vertical directions, respectively. In our simulations, like in the experiments [33,34], these parameters are kept fixed:

$$\Gamma_\phi = 4\pi \quad \text{and} \quad \Gamma_H = 1, \tag{2}$$

so that a vertical cross-section of the container has a square shape, $H = L = R/2$.

If the parameters of the experimental setup, including the physical container and the working fluid, are given, a dependent quantity A,

$$A \equiv \sqrt{\frac{4L^4 g_z}{\nu\kappa R}} = \frac{8\pi^2}{\Gamma_\phi^2}\sqrt{\frac{g_z R^3}{\nu\kappa}}, \tag{3}$$

is fixed as well. In the present DNS study, we aim to mimic the situation in the experiments, where the working fluid water is used and the size of the container is fixed by $R = 6$ cm or $R = 24$ cm, so that the quantity A is fixed as well in our study.

When $\Omega \neq 0$, the total acceleration that acts on a fluid in the considered CC system is a combination of both, the gravitational acceleration g_z (pointing downwards) and the centrifugal acceleration $g_\Omega \equiv \Omega^2 R$ (pointing outwards in the radial direction). Thus, in the CC system with $\Omega \neq 0$, the total acceleration that acts on the fluid is always larger than the acceleration due to gravity or centrifugation alone.

For a fixed maximal temperature difference Δ at the differently heated vertical surfaces of the container, a given distance L between them and a given fluid, which is characterized by the thermal expansion coefficient α, kinematic viscosity ν and thermal diffusivity κ, the total acceleration

$$\hat{g} \equiv \sqrt{g_z^2 + g_\Omega^2}, \qquad \text{where} \quad g_\Omega \equiv \Omega^2 R, \tag{4}$$

determines the main non-dimensional control parameter in the CC system, which is the Rayleigh number Ra, defined as

$$Ra \equiv \frac{\alpha \hat{g} L^3 \Delta}{\kappa\nu}. \tag{5}$$

The ratio between the momentum diffusion and thermal diffusion in the fluid gives the next control parameter, which is the Prandtl number Pr,

$$Pr \equiv \nu/\kappa. \tag{6}$$

In our simulations we keep $Pr = 4.3$, which corresponds to water at the temperature of about 40 °C.

Finally, there are two dimensionless control parameters that characterize rotation in the CC system, namely, the Rossby number Ro,

$$Ro \equiv \frac{\sqrt{\alpha \hat{g} L \Delta}}{2\Omega L}, \tag{7}$$

and the Froude number Fr,

$$Fr \equiv \frac{g_\Omega}{g_z} = \frac{\Omega^2 R}{g_z} = \frac{Ra}{A^2\, Ro^2}. \tag{8}$$

Thus, in the CC system, in addition to the two dimensionless geometrical parameters, Γ_ϕ and Γ_H, Eq. (1), we have other four dimensionless characteristics of the system:

- the ratio of the total buoyancy (a combination of the centrifugal buoyancy and gravitational buoyancy) to diffusion, reflected in the Rayleigh number Ra, Eq. (5);
- the ratio of momentum diffusion to heat diffusion, denoted as the Prandtl number Pr, Eq. (6);
- the ratio of the centrifugal buoyancy to gravitational buoyancy, reflected in the Froude number Fr, Eq. (8) ; and
- the ratio of the total buoyancy to rotation, characterized by the Rossby number Ro, Eq. (7).

[1] We consider a clockwise direction of the annulus rotation, similarly to the experiments in the ACRBC facility [33,34].

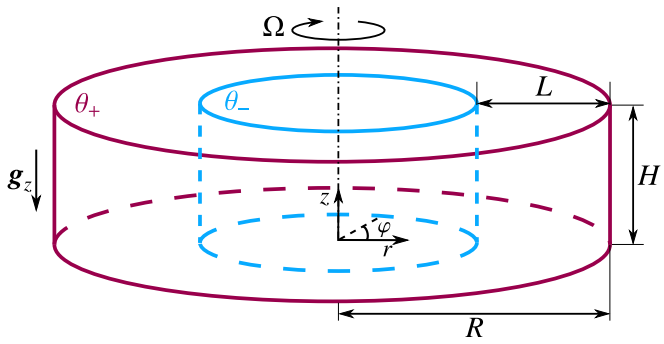

Fig. 1. Centrifugal convection (CC) setup considered in our simulations: an annular container with a height H, outer radius R, and distance L between the solid vertical walls, marked with blue and pink colours, is rotated clockwise about the vertical axis of the annulus at a constant angular velocity Ω. The container, which is confined between the two vertical (blue and pink) walls and the top and bottom horizontal solid walls separated by a distance H between them, is filled with a fluid. The outer and inner vertical walls are kept at temperatures θ_+ (pink) and θ_- (blue), respectively, where $\theta_+ > \theta_-$. The horizontal walls are fully thermally isolated and satisfy the adiabatic boundary conditions. The velocity at all vertical and horizontal walls satisfy the no-slip boundary conditions, $\boldsymbol{u} = 0$. (For interpretation of the references to colour in this figure legend, the reader is referred to the web version of this article.)

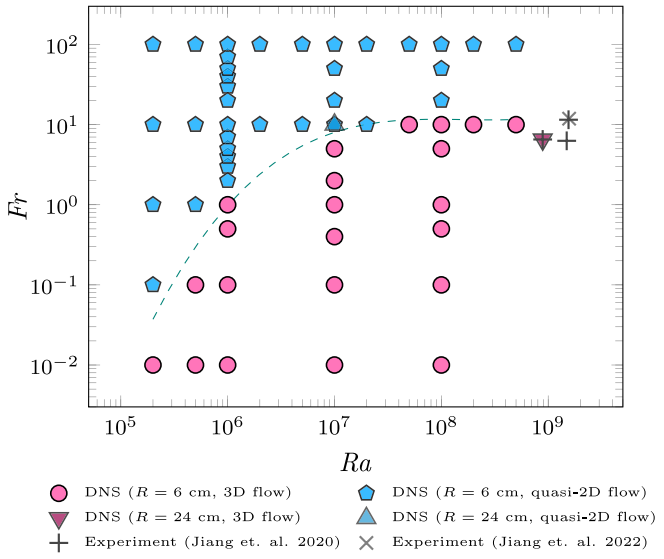

Fig. 2. Parameter diagram in the space of Rayleigh number (Ra) and Froude number (Fr) of the studied in direct numerical simulations (DNS) centrifugal convection (CC). Some experimental data adopted from Jiang et al. [33,34] are given for comparison. The pink data points correspond to three-dimensional flow structures obtained in the DNS (see the main text) and blue data to quasi-two-dimensional flow structures. The dashed line separates the two regimes and corresponds to the dashed line of Fig. 9a. (For interpretation of the references to colour in this figure legend, the reader is referred to the web version of this article.)

Note that alternatively one can take the Ekman number

$$Ek \equiv \frac{\nu}{2\Omega L^2} = Ro\sqrt{\frac{Pr}{Ra}} \tag{9}$$

as a control parameter, which is the ratio of the momentum diffusion to rotation.

Thus for fixed geometrical aspect ratios of the container, Γ_ϕ and Γ_H, we generally have four independent non-dimensional control parameters in the CC system: Ra, Pr, Fr, and Ro (or Ek). However, for a given container and a given fluid (i.e., when Γ_ϕ, Γ_H, A and Pr are fixed), the CC system has only two independent parameters, and we choose the Froude number and the Rayleigh number, to characterize the strengths of the centrifugal and gravitational buoyancy.

3. Governing equations and parameter range in direct numerical simulations

The dimensional governing equations within the Oberbeck–Boussinesq approximation in a rotating reference frame for an incompressible flow, accounting for the Coriolis, gravitational, and centrifugal buoyancy forces, include the following continuity equation, Navier–Stokes equation, and the temperature equation:

$$\nabla \cdot \boldsymbol{u} = 0, \tag{10}$$

$$D_t \boldsymbol{u} = -\frac{\nabla p}{\rho} + \nu\nabla^2\boldsymbol{u} + \alpha\theta g_z \boldsymbol{e}_z - 2\Omega\boldsymbol{u}\times\boldsymbol{e}_z - \alpha\theta\Omega^2 r\boldsymbol{e}_r, \tag{11}$$

$$D_t\theta = \kappa\nabla^2\theta, \tag{12}$$

where $D_t \equiv \partial_t + (\boldsymbol{u}\cdot\nabla)$ denotes the material derivative, p is the pressure, $\boldsymbol{u}$ the velocity vector field, θ the temperature (reduced by the arithmetic mean of the smallest and largest temperatures at the boundaries of the container), and ρ is the fluid density. Further, Ω is the rotation rate, g_z is the acceleration due to gravity, $\boldsymbol{e}_z$ the unit vector in the vertical z-direction, $\boldsymbol{e}_r$ the unit vector in the radial r-direction of the annulus. In the right-hand side of the Eq. (11), the last three therms correspond to the gravitational buoyancy ($\alpha\theta g_z\boldsymbol{e}_z$), Coriolis force ($-2\Omega\boldsymbol{u}\times\boldsymbol{e}_z$) and the centrifugal force ($-\alpha\theta\Omega^2 r\boldsymbol{e}_r$).

The boundary conditions are no-slip for the velocity at all vertical and horizontal walls,

$$\boldsymbol{u}|_{z=0} = 0, \qquad \boldsymbol{u}|_{z=H} = 0, \tag{13}$$

$$\boldsymbol{u}|_{r=R} = 0, \qquad \boldsymbol{u}|_{r=R-L} = 0, \tag{14}$$

adiabatic at the top and bottom surfaces,

$$\partial_z\theta\big|_{z=0} = 0, \quad \partial_z\theta\big|_{z=H} = 0, \tag{15}$$

and isothermal at the vertical side walls,

$$\theta|_{r=R} = \theta_+, \quad \theta|_{r=R-L} = \theta_-, \tag{16}$$

where $\Delta \equiv \theta_+ - \theta_- > 0$.

To account for the centrifugal buoyancy dominance for some parameter ranges and for the gravitational buoyancy dominance for other parameter ranges in our simulations, we propose a new way of non-dimensionalizing the governing equations. Precisely, to non-dimensionalize Eqs. (10)–(12), the following reference scales were chosen for length, velocity and time, respectively: the outer radius R, the free-fall velocity $\hat{u}_{\mathrm{ff}} \equiv \sqrt{\alpha\hat{g}R\Delta}$, and the free-fall time $R/\sqrt{\alpha\hat{g}R\Delta}$, where $\hat{g} \equiv \sqrt{g_z^2 + g_\Omega^2}$ is the total acceleration and $g_\Omega \equiv \Omega^2 R$ the centrifugal acceleration.[2] The temperature θ is non-dimensionalized by the temperature difference $\Delta \equiv \theta_+ - \theta_-$ between outer and inner cylinders, and pressure p by $\rho\alpha\hat{g}R\Delta$.

The non-dimensional governing equations take then the following form:

$$\nabla \cdot \boldsymbol{u} = 0, \tag{17}$$

$$D_t\boldsymbol{u} = -\nabla p + \sqrt{\frac{8\pi^3}{\Gamma_\phi^3}\frac{Pr}{Ra}}\nabla^2\boldsymbol{u} + \frac{1}{\sqrt{1+Fr^2}}\theta\boldsymbol{e}_z - \sqrt{\frac{\Gamma_\phi}{2\pi}}Ro^{-1}\boldsymbol{u}\times\boldsymbol{e}_z - \frac{Fr}{\sqrt{1+Fr^2}}\theta r\boldsymbol{e}_r, \tag{18}$$

$$D_t\theta = \sqrt{\frac{8\pi^3}{\Gamma_\phi^3\, Pr\, Ra}}\nabla^2\theta, \tag{19}$$

where, for simplicity, we use the same notations for the dimensionless velocity, temperature and pressure, as previously, in the corresponding dimensional Eqs. (10)–(12).

As discussed, for fixed geometrical aspect ratios of the container, Γ_ϕ and Γ_H, the nondimensional control parameters in the CC system are the Rayleigh number Ra, Prandtl number Pr, Froude number Fr, and Rossby number Ro. However, if the fluid and the size of the container are given, then the system has only two control parameters, and we choose the Froude number and the Rayleigh number.

In all our simulations we take water at the temperature of about 40 °C as a working fluid, leading to $Pr = 4.3$ in all DNS. In most of our DNS, we consider the annulus container with the outer radius $R = 6$ cm, and only for two cases we have the radius $R = 24$ cm, as in the ACRBC facility [33,34]. Therefore, the value of A, Eq. (3), and the Prandtl number are considered as given, and the Rossby number becomes a dependent parameter that can be calculated from A, Fr and Ra, cf. Eq. (8). Under these conditions, the remaining control parameters are only Ra and Fr.

In Fig. 2 the parameter diagram of all conducted DNS is given. As one can see, the studied Ra-range spans over four decades, and the Fr-range over five decades. In Fig. 2 we also mark some data points from Jiang et al. [33,34] for the accessible in the present DNS parameter range.

To conduct direct numerical simulations of CC, we have advanced the latest version of our fourth-order in space and third-order Runge–Kutta in time finite-volume computational code GOLDFISH[55–58] to an annular geometry, similarly as it was done in our previous work [59] (to account for the presence of heated and cooled obstacles inside the convection cell, or, in other words, the presence of internal boundaries inside the domain), and to account for rotation [60–63] and specific boundary conditions, as it was done in [64,65], with additional care on the centrifugal effects.

Our DNS use sufficiently fine computational grids, which are non-uniform in the r- and z- directions, being denser close to the boundaries compared to the bulk. The grids resolve the Kolmogorov microscales

$$\eta_K \equiv (\nu^3/\epsilon_u)^{1/4} \tag{20}$$

and Batchelor microscales

$$\eta_B \equiv (\nu\kappa^2/\epsilon_u)^{1/4} = \eta_K\, Pr^{-1/2} \tag{21}$$

within the bulk flow and in the boundary layers, according to the requirements from Shishkina et al. [66]. Here ϵ_u is the kinetic energy dissipation rate. Since we consider only large Prandtl number case, the requirement to resolve the Batchelor microscale is the most restrictive. In addition, to ensure the quality of the computational mesh, a grid refinement study has been performed for selected cases, where the change of the grid resolution by a factor of at least 2.5 resulted in changes of the Nusselt number Nu (dimensionless convective heat transport, discussed later), by less than 1%, over a long-time average.

4. Results of the direct numerical simulations

Based on the results of our direct numerical simulations (DNS), here we investigate flow structures and heat transport in the above discussed CC setup for various thermal driving (Ra) and rotation (Fr) parameters. In our study, the largest considered Ra value corresponds to the lower boundary of the Ra-range studied experimentally at the ACRBC facility [33]. However, here we mainly focus on flow regimes of smaller Rayleigh number Ra and investigate, how the flow structures change with changing Froude number Fr. This includes the cases, where the gravity acceleration cannot be neglected and the flow is rather a mixture of vertical convection and Rayleigh–Bénard convection. We explore the key features of CC and demonstrate the evolution of the CC flow with increasing contribution of the centrifugal acceleration, starting from its gravitational buoyancy dominated regime (which is similar to vertical convection) and up to the regime of the centrifugal buoyancy dominance (which is similar to Rayleigh–Bénard convection).

The parameter space of the conducted DNS with rotation ($Fr > 0$) is sketched in Fig. 2. For reference, we also have conducted DNS without rotation ($Fr = 0$) for some Rayleigh numbers ($Ra = 2\times10^5$, 5×10^5, 10^6, 10^7 and 10^8). The main simulation parameters and key response characteristics are summarized in Table A.1 of Appendix A.2.

In all our DNS, we consider as working fluid water at the temperature 40 °C so that all fluid properties, including the Prandtl number $Pr = 4.3$, are assumed to be fixed. Moreover, the geometrical aspect ratio parameters of the container are also given, $\Gamma_\phi = 4\pi$ and $\Gamma_H = 1$. In order to leave only two control parameters (Ra and Fr), it is sufficient to fix in addition only one characteristic that determined the physical size of the container (see the discussion in Section 2), for example, the outer radius R. In other words, if the fluid and the physical container are given, then the remaining control parameters of the CC system are only the temperature difference Δ and rotation rate Ω, which in dimensionless quantities is reflected in the control parameters Rayleigh number Ra, Eq. (5), and Froude number Fr, Eq. (8).

From Eqs. (3) and (8) one can see that for given Ra and Fr, the inverse Rossby number is proportional to $R^{3/2}$, therefore the larger the physical size of the container is, the more challenging the simulations of the CC flow in such container are, see the governing equations (17)–(19). In the ACRBC facility [33,34], the outer radius is equal to $R = 24$ cm. To study in the DNS the Fr-dependence of CC for given Ra-values and the same time make the simulations feasible, we have fixed $R = 6$ cm in our virtual container, for most of our simulations, see Table A.1 of Appendix A.2.

However, to make a connection to the experiments in the ACRBC facility [33,34], we also conducted two DNS for the $R = 24$ cm case, which results are reported at the bottom of Table A.1 of Appendix A.2.

[2] We use as the reference distance the radius R, and not the gap L between the vertical walls, since the main driving acceleration, g_Ω, depends on the radius.

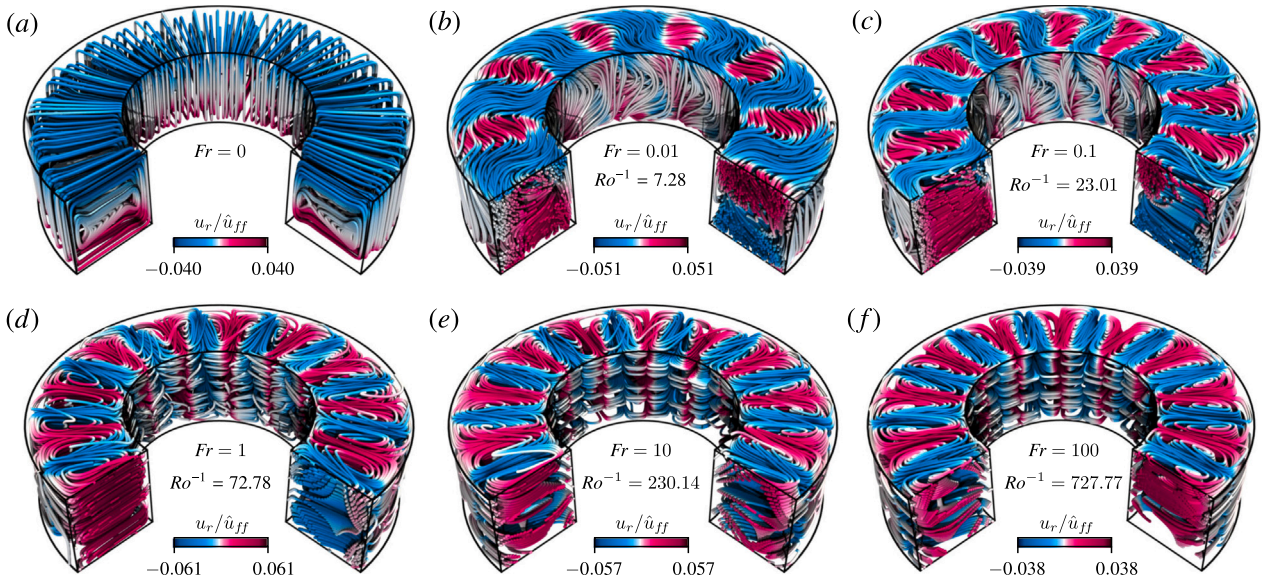

Fig. 3. Instantaneous flow fields, visualized with trajectories of passive tracer particles, coloured by the values of the radial velocity component u_r (normalized with $\hat{u}_{\mathrm{ff}} \equiv \sqrt{\alpha \hat{g} R \Delta}$, where $\hat{g} \equiv \sqrt{g_z^2 + \Omega^4 R^2}$), as obtained in the DNS for $Ra = 10^6$ ($R = 6$ cm). For clarity, only 3/4 of the domain is shown. (For interpretation of the references to colour in this figure legend, the reader is referred to the web version of this article.)

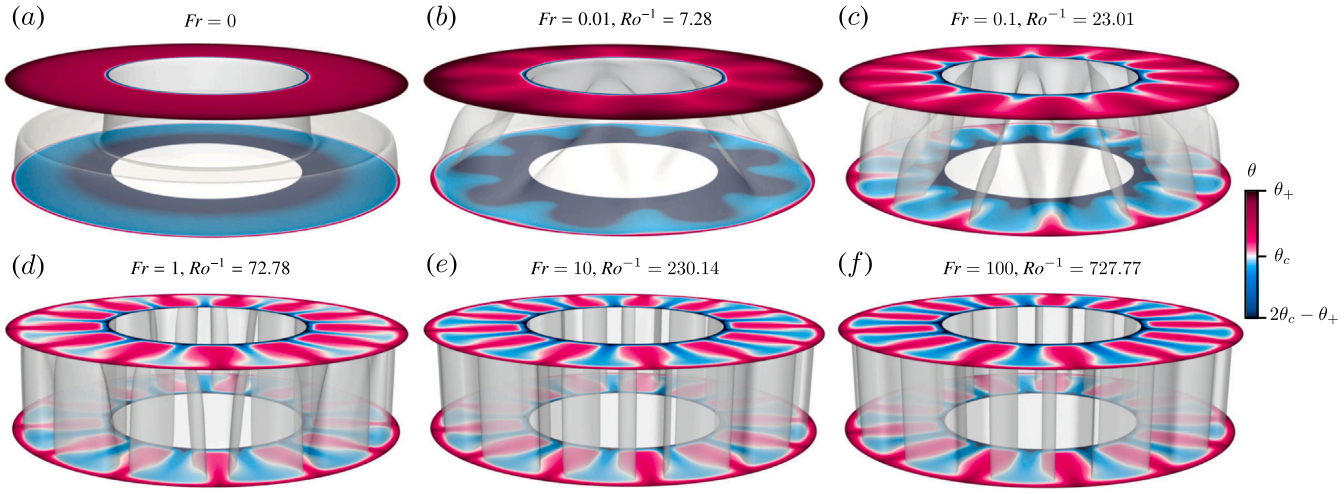

Fig. 4. Instantaneous temperature distributions at the bottom ($z/H = 0$) and top ($z/H = 1$) walls together with the temperature isosurfaces that correspond to the volume-averaged temperature of the fluid in the pure conduction case ($\theta_c/\Delta \approx 0.112$), as obtained in the DNS for $Ra = 10^6$ ($R = 6$ cm) and different Froude numbers and inverse Rossby numbers (see the legend). The colour scale ranges from blue (that corresponds to the temperature $\theta = 2\theta_c - \theta_+$) through white ($\theta = \theta_c$) to pink ($\theta = \theta_+$). (For interpretation of the references to colour in this figure legend, the reader is referred to the web version of this article.)

One of these DNS was conducted for $Ra = 8.88 \times 10^8$, $Fr = 6.53$ and $Ro^{-1} = 49.94$ ($R = 24$ cm) and corresponds to the lower parameter range of the experimental study by Jiang et al. [33]. This simulation gives an idea of the flow structures inside the ACRBC facility. The other DNS, conducted for $Ra = 10^7$, $Fr = 10$ and $Ro^{-1} = 582.22$ ($R = 24$ cm), allows us to compare the flows for the same Ra and Fr, but different Ro (or, in other words, for different sizes of the container). Namely, we make a comparison with the also simulated case $Ra = 10^7$, $Fr = 10$ and $Ro^{-1} = 72.78$ ($R = 6$ cm).

4.1. Flow structure

In Figs. 3–8 we present instantaneous flow structures obtained in our DNS for the container with $R = 6$ cm, for different Rayleigh numbers: $Ra = 10^6$ in Figs. 3–4, $Ra = 10^7$ in Figs. 5–6, and $Ra = 10^8$ in Figs. 7–8, and varying Froude numbers.

Figs. 3, 5 and 7 show instantaneous flow fields visualized with trajectories of passive tracer particles and coloured by the values of the radial velocity u_r, so that the blue colour reflects the fluid motion towards the centreline of the annulus and pink colour indicates the flow away from the centreline.

The flows without imposed rotation, $Fr = 0$, see Figs. 3a, 5a and 7a, show a clear flow structure typical for vertical convection, where the fluid moves upwards near the heated outer vertical wall and moves downwards near the cooled vertical wall, forming a large-scale circulation, so that the fluid moves towards the centreline in the upper half of the container and in the opposite direction in the lower part of the container. There is almost no mixing in the azimuthal direction ϕ, therefore the flow can be considered as quasi-two-dimensional, varying only in the r- and z-directions. In this extreme case, $Fr = 0$, exclusively gravitational acceleration g_z determines buoyant processes in the system.

The other extreme case is the case of very large Fr, where the centrifugal buoyancy dominates over gravitational buoyancy, and the

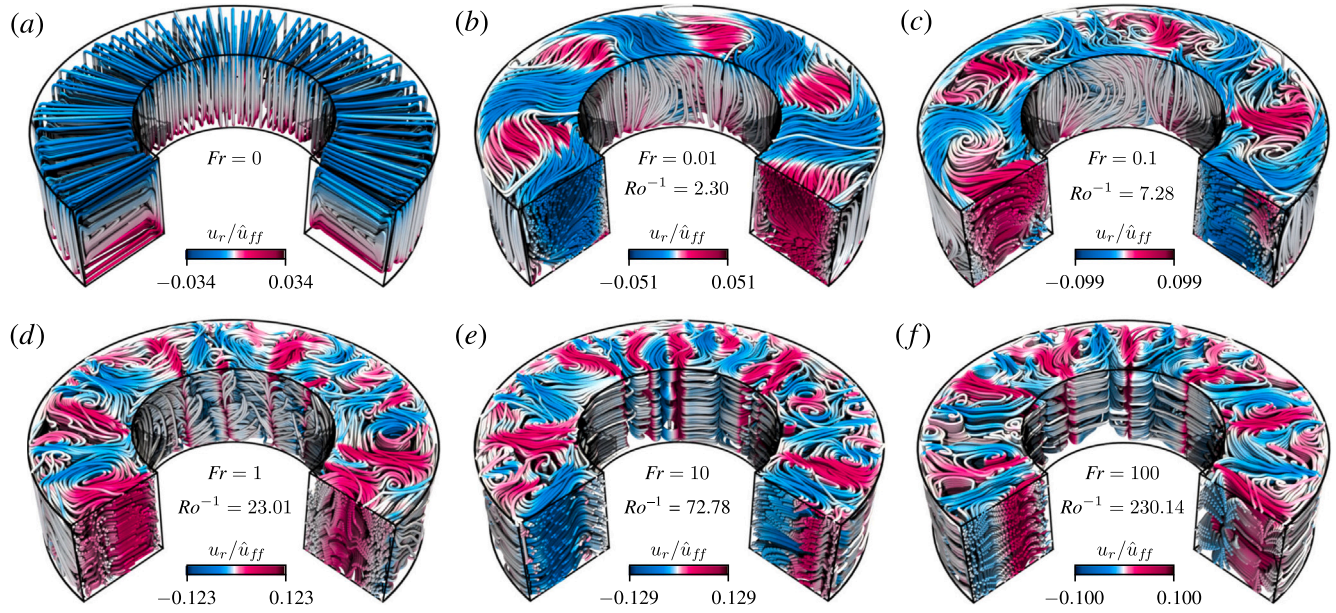

Fig. 5. Instantaneous flow fields, visualized with trajectories of passive tracer particles, coloured by the values of the radial velocity component u_r (normalized with $\hat{u}_{\mathrm{ff}} \equiv \sqrt{\alpha \hat{g} R \Delta}$, where $\hat{g} \equiv \sqrt{g_z^2 + \Omega^4 R^2}$), as obtained in the DNS for $Ra = 10^7$ ($R = 6$ cm). For clarity, only 3/4 of the domain is shown. (For interpretation of the references to colour in this figure legend, the reader is referred to the web version of this article.)

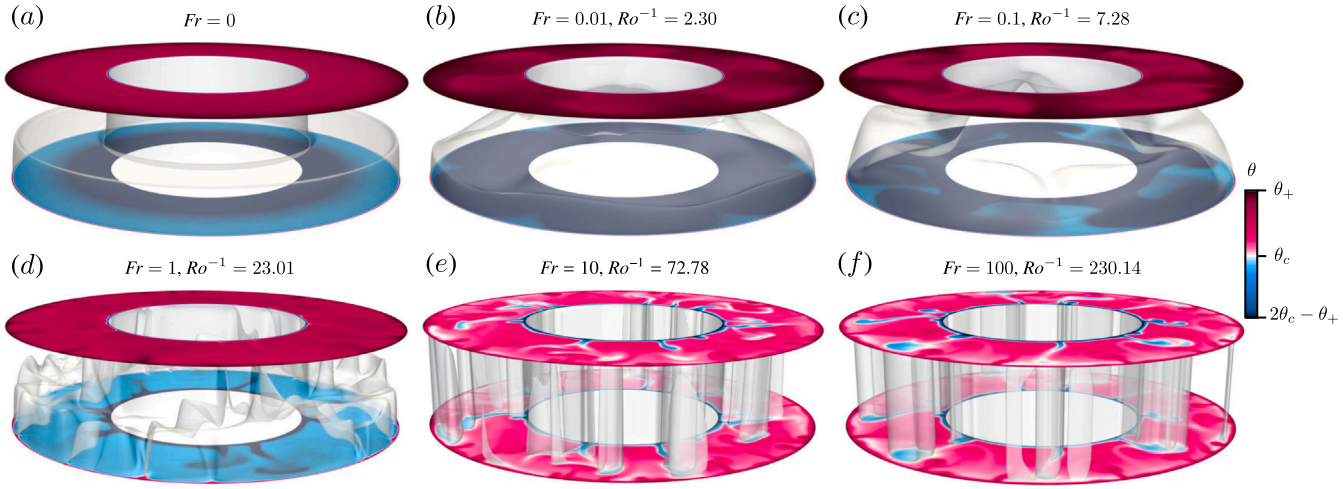

Fig. 6. Instantaneous temperature distributions at the bottom ($z/H = 0$) and top ($z/H = 1$) walls together with the temperature isosurfaces that correspond to the volume-averaged temperature of the fluid in the pure conduction case ($\theta_c/\Delta \approx 0.112$), as obtained in the DNS for $Ra = 10^7$ ($R = 6$ cm) and different Froude numbers and inverse Rossby numbers (see the legend). The colour scale ranges from blue (that corresponds to the temperature $\theta = 2\theta_c - \theta_+$) through white ($\theta = \theta_c$) to pink ($\theta = \theta_+$). (For interpretation of the references to colour in this figure legend, the reader is referred to the web version of this article.)

contribution of the gravitational acceleration g_z becomes negligible in the total acceleration $\hat{g} \equiv \sqrt{g_z^2 + g_\Omega^2}$, where $g_\Omega \equiv \Omega^2 R$. This case is illustrated in Figs. 3f, 5f and 7f, where the flow fields for $Fr = 100$ are plotted. The CC system then resembles Rayleigh–Bénard convective system "lying on a side", so that the typical convection rolls are built about vertical axes, and the turbulent mixing of the fluid in the vertical direction is suppressed. Thus, in the other extreme case of $Fr \to \infty$, where now the centrifugal acceleration g_Ω determines the buoyant processes in the system, the flow is again quasi-two-dimensional, however, now varying in the r- and ϕ-directions.

When for a fixed Rayleigh number, the Froude number changes from 0 to 100, the flow is first quasi-two-dimensional, with suppressed motion in the ϕ-direction, then becomes fully three-dimensional, since rotation supports the motion in the ϕ-direction as well, and finally, with further increase of Fr, the flows become again quasi-two-dimensional since the motion in the z-direction gets suppressed by strong rotation, according to the Taylor–Proudman theorem. This evolution of the flow with growing Fr is clearly seen in Fig. 3(a–f) for $Ra = 10^6$, Fig. 5(a–f) for $Ra = 10^7$, and Fig. 7(a–f) for $Ra = 10^8$.

If we focus only on the flows where the centrifugal buoyancy is influential or determining, then the transition from the fully three-dimensional flow to quasi-two-dimensional flow can be identified by evaluating the relative strength of the vertical motion, $\langle u_z^2 \rangle_{V,t}^{1/2} / \hat{u}_{\mathrm{ff}}$, as a function of either the Froude number or inverse Rossby number. In Fig. 9, this quantity is plotted as functions of Fr and Ro^{-1}, for different Rayleigh numbers Ra. One can see that starting a certain Fr or Ro^{-1}, the relative contribution of the vertical velocity gets small. We used a threshold $\langle u_z^2 \rangle_{V,t}^{1/2} / \hat{u}_{\mathrm{ff}} < 10^{-3}$ to identify the quasi-two-dimensional flows, which are marked blue in Fig. 2. (Pink data points in Fig. 2 correspond to three-dimensional flow structures).

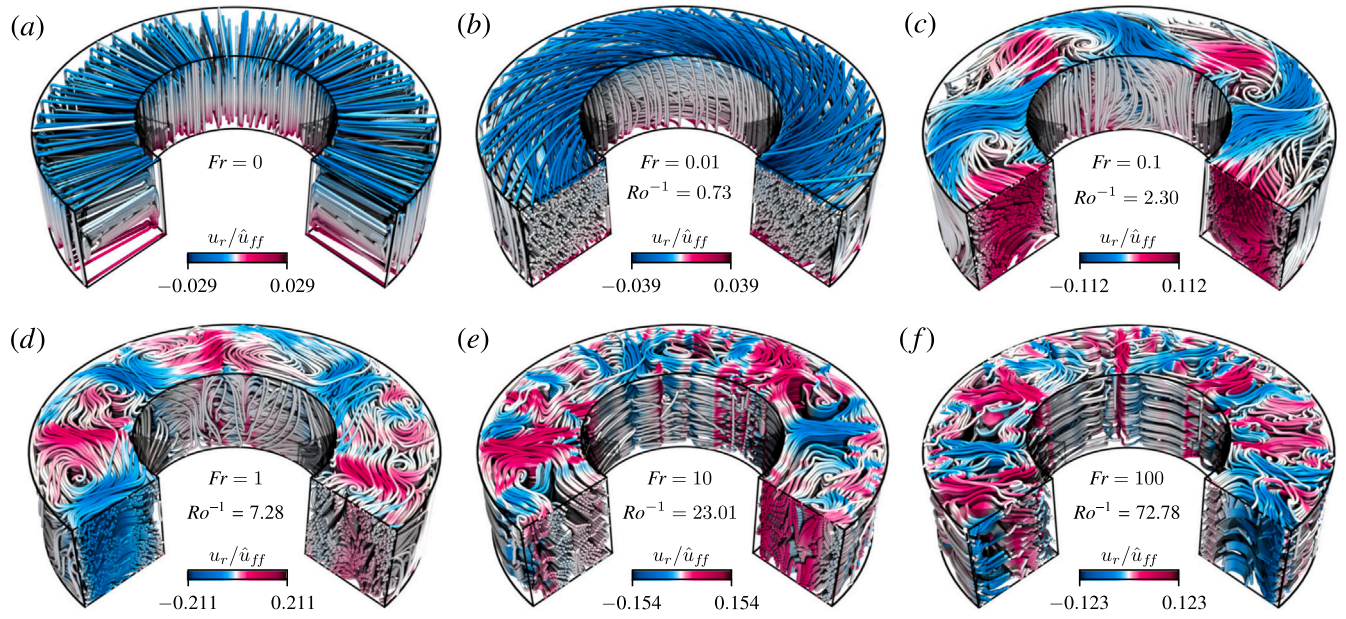

Fig. 7. Instantaneous flow fields, visualized with trajectories of passive tracer particles, coloured by the values of the radial velocity component u_r (normalized with $\hat{u}_{\mathrm{ff}} \equiv \sqrt{\alpha \hat{g} R \Delta}$, where $\hat{g} \equiv \sqrt{g_z^2 + \Omega^4 R^2}$), as obtained in the DNS for $Ra = 10^8$ ($R = 6$ cm). For clarity, only 3/4 of the domain is shown. (For interpretation of the references to colour in this figure legend, the reader is referred to the web version of this article.)

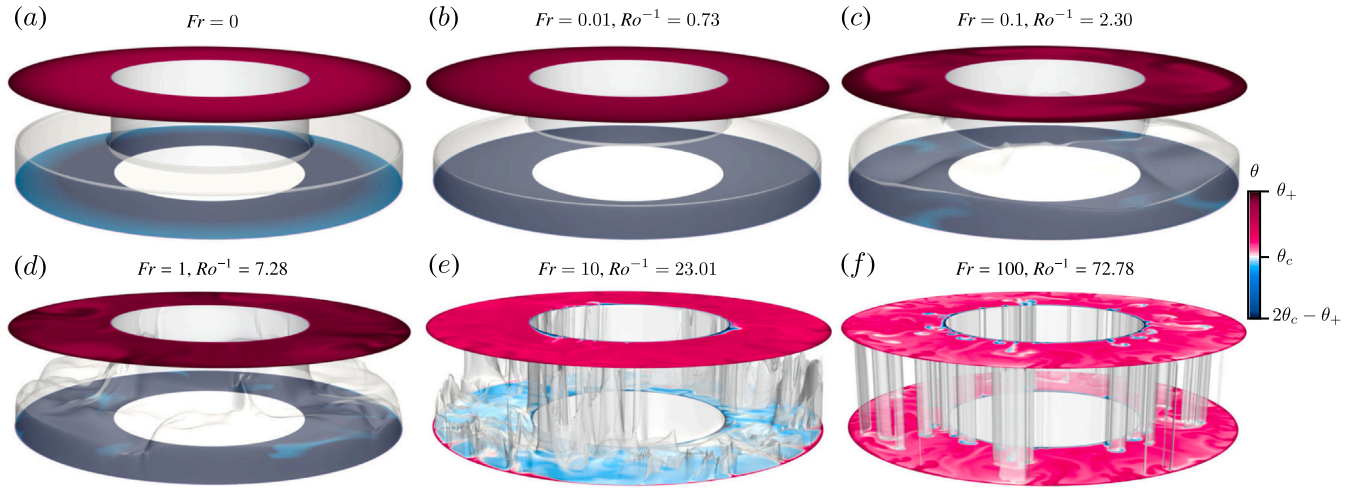

Fig. 8. Instantaneous temperature distributions at the bottom ($z/H = 0$) and top ($z/H = 1$) walls together with the temperature isosurfaces that correspond to the volume-averaged temperature of the fluid in the pure conduction case ($\theta_c/\Delta \approx 0.112$), as obtained in the DNS for $Ra = 10^8$ ($R = 6$ cm) and different Froude numbers and inverse Rossby numbers (see the legend). The colour scale ranges from blue (that corresponds to the temperature $\theta = 2\theta_c - \theta_+$) through white ($\theta = \theta_c$) to pink ($\theta = \theta_+$). (For interpretation of the references to colour in this figure legend, the reader is referred to the web version of this article.)

4.2. Temperature distribution

Now we consider the instantaneous temperature distributions, which are presented in Figs. 4, 6 and 8, for $Ra = 10^6$, $Ra = 10^7$, and $Ra = 10^8$, respectively. The changes of the temperature distributions for a fixed Ra and growing Fr are fully consistent with the changes in the corresponding flow structures in Figs. 3, 5, and 7 and reflect the transitions from the quasi-two-dimensional to three-dimensional and then again, another quasi-two-dimensional global flow structures. For larger Ra, the flows certainly exhibit more fluctuations and thermal plumes in the three-dimensional regime, however, the evolution from the no-rotation case ($Fr = 0$, vertical convection, dominance of gravitational buoyancy) to the strong rotation case ($Fr = 100$, quasi-Rayleigh–Bénard convection, dominance of centrifugal buoyancy) is similar in all studied Ra-cases.

In Oberbeck–Boussinesq centrifugal convection, the time- and volume averaged temperature is always larger than the arithmetic mean of the temperatures at the vertical heated and cooled surfaces, which is very different to the classical Rayleigh–Bénard convection, where the bulk temperature equals the arithmetic mean of the top and bottom temperatures.

This phenomena (“too warm” bulk) becomes apparent already in the purely conductive case and is explained by the geometry of the container. Indeed, in the absence of any fluid motion, the temperature

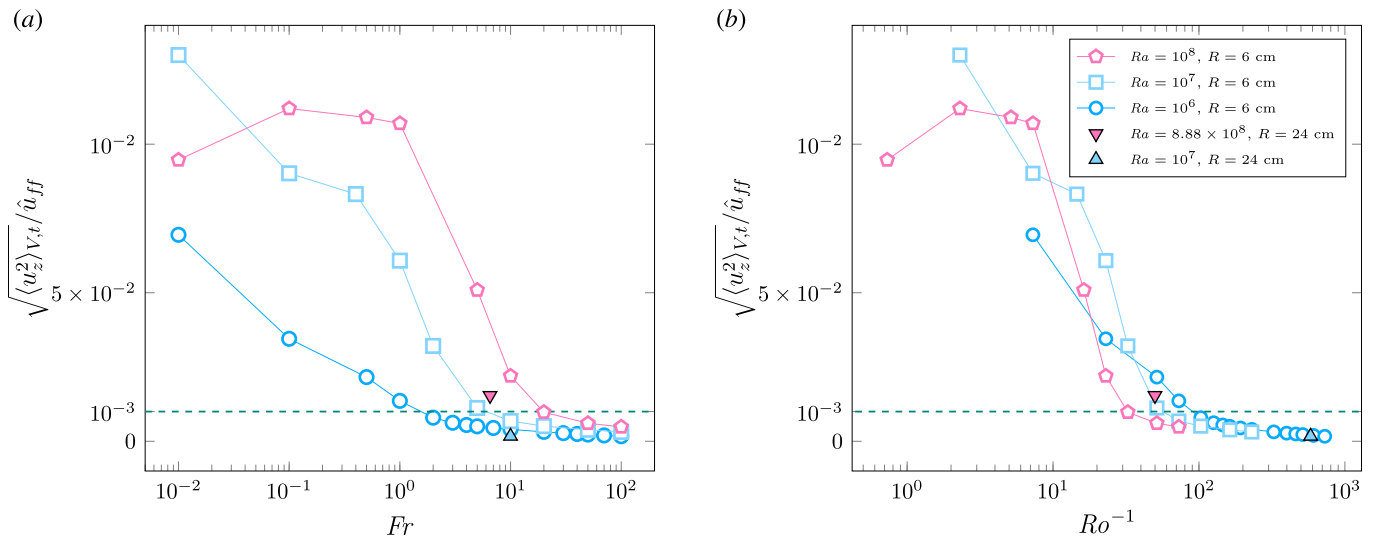

Fig. 9. Relative strength of the vertical motion, as functions of (a) the Froude number Fr and (b) inverse Rossby number Ro^{-1}, for different Rayleigh numbers Ra. Both figures share the same legend given in (b). (For interpretation of the references to colour in this figure legend, the reader is referred to the web version of this article.)

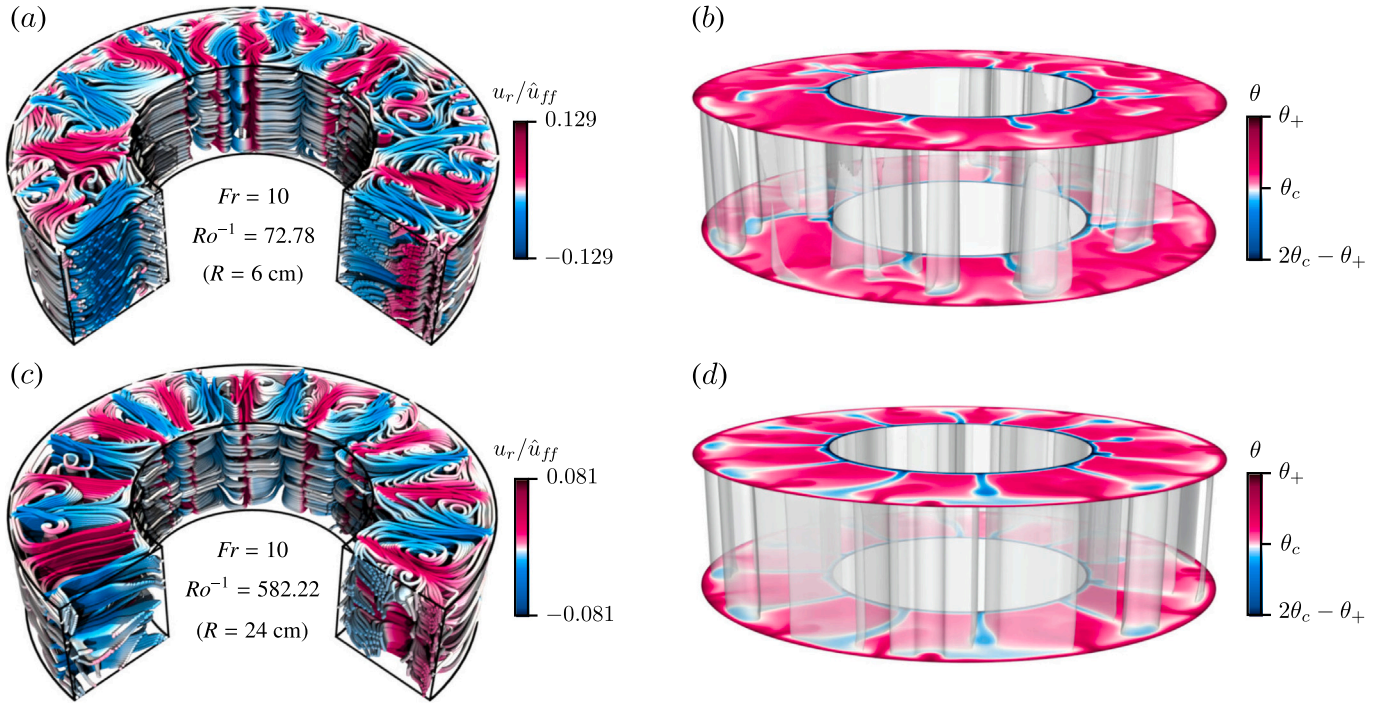

Fig. 10. A comparison of the flow structures for the same $Ra = 10^7$, $Fr = 10$, but different sizes of the container: (a, b) $R = 6$ cm and (c, d) $R = 24$ cm, as obtained in the DNS. The instantaneous flow fields are visualized with (a, c) trajectories of passive tracer particles, coloured by the values of the radial velocity u_r (normalized with $\hat{u}_{\mathrm{ff}} \equiv \sqrt{\alpha \hat{g} R \Delta}$, where $\hat{g} \equiv \sqrt{g_z^2 + \Omega^4 R^2}$) and (b, d) instantaneous temperature distributions at the bottom ($z/H = 0$) and top ($z/H = 1$) walls together with the isosurfaces that correspond to the mean temperature of the fluid in the pure conduction case ($\theta_c/\Delta \approx 0.112$). For clarity, only 3/4 of the domains are shown in (a, c). (For interpretation of the references to colour in this figure legend, the reader is referred to the web version of this article.)

equation (12) is reduced to the following equation in cylindrical coordinates:

$$\frac{1}{r}\partial_r(r\partial_r\theta) = 0 \tag{22}$$

with the solution

$$\theta = \theta_- + \Delta\frac{\log\frac{r}{R-L}}{\log\frac{R}{R-L}}. \tag{23}$$

Obviously, the temperature profile in the conductive case of the CC setup is not linear (in contrast to the conductive case in the classical Rayleigh–Bénard setup). Introducing the mean bulk temperature in the pure conduction case as

$$\theta_c \equiv \langle\theta\rangle_V \tag{24}$$

and integrating the temperature equation (23) in the entire domain, we obtain the bulk temperature in the pure conduction case:

$$\theta_c = \frac{2}{(R^2-(R-L)^2)}\int_{R-L}^{R}\left(\theta_- + \Delta\frac{\log\frac{r}{R-L}}{\log\frac{R}{R-L}}\right) r\,dr, \tag{25}$$

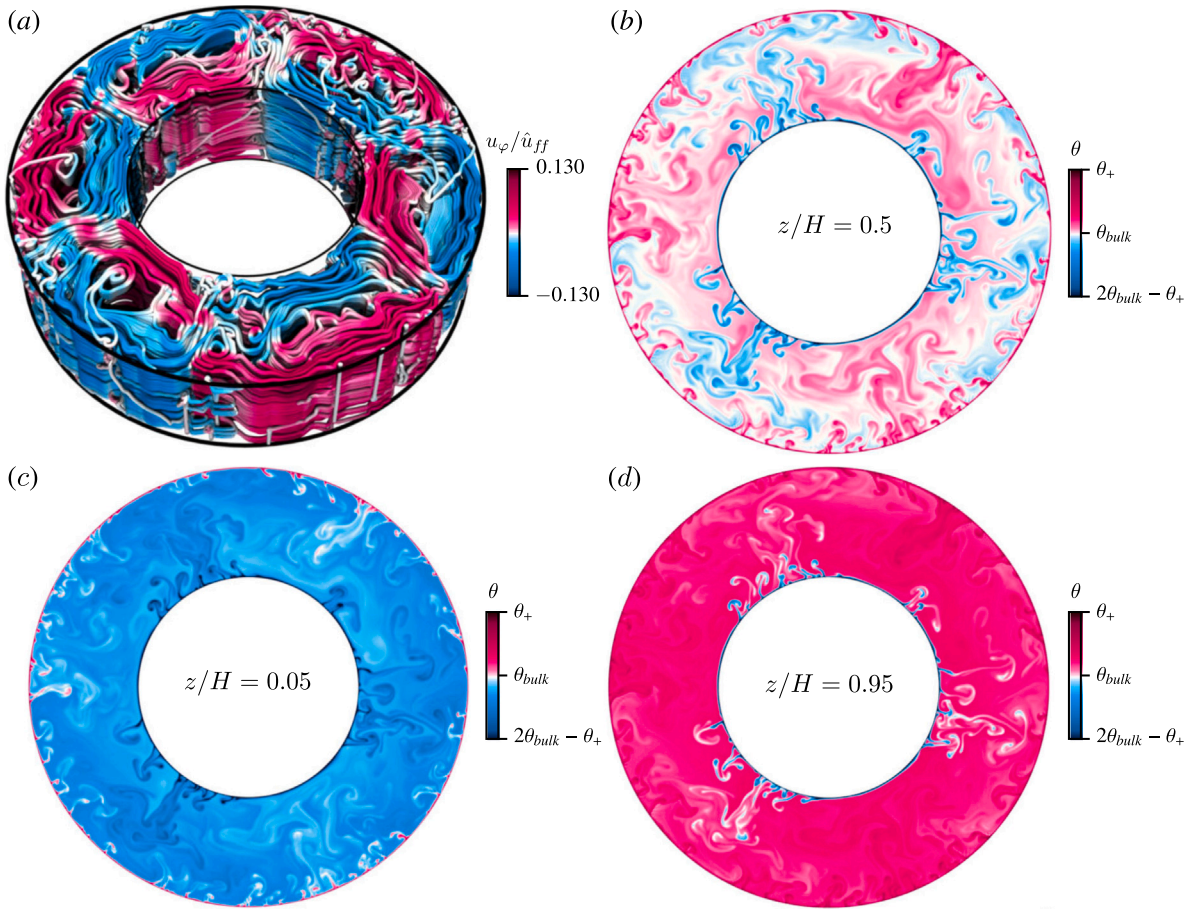

Fig. 11. Obtained in our DNS instantaneous flow structure for $Ra = 8.88 \times 10^8$, $Fr = 6.53$, $Ro^{-1} = 49.94$ ($R = 24$ cm) visualized with (a) trajectories of passive tracer particles, coloured by the values of the azimuthal velocity u_ϕ (normalized with $\hat{u}_{\rm ff} \equiv \sqrt{\alpha \hat{g} R \Delta}$, where $\hat{g} \equiv \sqrt{g_z^2 + \Omega^4 R^2}$) and (b–d) horizontal cross-sections of the temperature field considered at (b) $z/H = 0.5$ (at the mid plane), (c) $z/H = 0.05$ (close to the bottom), and (d) $z/H = 0.95$ (close to the top). White colour corresponds to the time- and volume-averaged temperature of the fluid, which is $\theta_{\rm bulk}/\Delta \approx 0.18$. The case $Ra = 8.88 \times 10^8$, $Fr = 6.53$, $Ro^{-1} = 49.94$ presented here corresponds to one experimentally studied case ($R = 24$ cm) from Jiang et al. [33] and is marked with a pink filled triangle in Figs. 2 and 12. (For interpretation of the references to colour in this figure legend, the reader is referred to the web version of this article.)

which can be reduced to

$$\frac{\theta_c}{\Delta} = -\frac{1}{2} + \frac{1}{2\log(1 - 2\pi\Gamma_\phi^{-1})} + \frac{\Gamma_\phi^2}{4\pi\Gamma_\phi - 4\pi^2}. \tag{26}$$

In the $\Gamma_\phi \to \infty$ limit, the container curvature does not matter anymore, and $\theta_c/\Delta \to 0$, as expected, meaning that the bulk temperature is equal to the arithmetic mean of the temperatures of the heated and cooled vertical walls of the container. In the other limit, $\Gamma_\phi \to 2\pi$, when the inner vertical wall approaches the container centreline, the bulk temperature tends to the temperature of the hottest outer vertical wall, $\theta_c/\Delta \to 1/2$. In the intermediate case $\Gamma_\phi = 4\pi$ that was considered in the experimental study by Jiang et al. [33,34] and in our DNS, the bulk temperature in the case of pure conduction equals

$$\frac{\theta_c}{\Delta} = \frac{5}{6} - \frac{1}{2\log 2} \approx 0.112. \tag{27}$$

Exactly this value $\theta_c/\Delta \approx 0.112$ is used as a reference value that corresponds to the white colour in Figs. 4, 6 and 8, to visualize the temperature distributions.

For each studied case, the time and volume-averaged dimensionless temperature of the fluid, $\theta_{\rm bulk}/\Delta$, is given in Table A.1 of Appendix A.2. For laminar cases we have

$$\theta_{\rm bulk} \approx \theta_c, \tag{28}$$

however, with increasing centrifugal buoyancy (Fr and Ra), the bulk temperature further increases, $\theta_{\rm bulk} > \theta_c$.

For highly turbulent CC, with $Fr \gg 1$, the bulk becomes almost isothermal, and for this case Wang et al. [67] proposed a model to predict the bulk temperature, which is based on the following assumptions. Within the thermal boundary layer of the thickness λ_i (λ_o) next to the inner (outer) vertical wall, the temperature change is Δ_i (Δ_o), so that

$$\Delta_i + \Delta_o = \Delta. \tag{29}$$

The areas of the two vertical walls are different, but the same amount of heat is transported across the both surfaces, therefore

$$\frac{\Delta_i}{\lambda_i}(R - L) = \frac{\Delta_o}{\lambda_o} R. \tag{30}$$

And finally, in analogy to the non-Oberbeck–Boussinesq model by Wu and Libchaber [68], in Wang et al. [67], it is assumed that the temperature scales for the both boundary layers are equal:

$$\frac{\nu\kappa}{\alpha g_i \lambda_i^3} = \frac{\nu\kappa}{\alpha g_o \lambda_o^3}, \tag{31}$$

where $g_i = \Omega^2(R - L)$ and $g_o = \Omega^2 R$. A combination of Eqs. (29)–(31) and (1) leads to a conclusion that both, the thickness of the outer thermal boundary layer and the temperature drop within this boundary

layer are smaller than the corresponding quantities of the inner thermal boundary layer:

$$\frac{\lambda_o}{\lambda_i} = \left(1 - \frac{L}{R}\right)^{1/3} = \left(1 - \frac{2\pi}{\Gamma_\phi}\right)^{1/3} < 1 \tag{32}$$

and

$$\frac{\Delta_o}{\Delta_i} = \left(1 - \frac{L}{R}\right)^{4/3} = \left(1 - \frac{2\pi}{\Gamma_\phi}\right)^{4/3} < 1. \tag{33}$$

The bulk temperature in the highly turbulent regime with $Fr \gg 1$ is then estimated as

$$\frac{\theta_{\text{bulk}}}{\Delta} = \frac{\Delta_i}{\Delta} - \frac{1}{2} = \frac{1}{(1 - L/R)^{4/3} + 1} - \frac{1}{2} = \frac{1}{(1 - 2\pi/\Gamma_\phi)^{4/3} + 1} - \frac{1}{2}, \tag{34}$$

which for the considered geometry with $L/R = 1/2$ gives the following estimate of the bulk temperature:

$$\frac{\theta_{\text{bulk}}}{\Delta} \approx 0.216, \tag{35}$$

see [67]. Our simulations show that indeed, when both, Ra and Fr are large, the bulk temperature approaches this value, see Table A.1 for $Ra = 5 \times 10^8$ and $Fr = 100$, for which we obtained $\theta_{\text{bulk}}/\Delta \approx 0.206$.

Note that the functions $1/(x^{4/3}+1) - 1/2$ and $(1-x)/2$ are sufficiently close to each other in the interval $x \in [0, 1]$, therefore the bulk temperature in the highly turbulent regime with $Fr \gg 1$ can be sufficiently well approximated by the following simple formula:

$$\frac{\theta_{\text{bulk}}}{\Delta} \approx \frac{\pi}{\Gamma_\phi}, \tag{36}$$

cf. Eq. (34). Eq. (36) reflects also that when the inner vertical wall is very close to the centreline of the domain ($\Gamma_\phi \to 2\pi$), the bulk temperature is close to the temperature of the outer hot vertical wall ($\theta_{\text{bulk}} \approx \Delta/2$), while in the case of a small gap between the vertical walls compared to the outer radius ($\Gamma_\phi \to \infty$), the bulk temperature is close to the arithmetic mean of the temperatures of the two vertical walls.

4.3. The effect of the container size

As mentioned above, most of our DNS were conducted at a fixed value of $R = 6$ cm, while the measurements by Jiang et al. [33,34] were conducted in the ACRBC facility with the radius $R = 24$ cm. To investigate the effect of the facility size on the flow structure and transport properties, we conducted DNS for the same $Ra = 10^7$ and $Fr = 10$, but different radii: $R = 6$ cm and $R = 24$ cm, which correspond to different inverse Rossby numbers: $Ro^{-1} \approx 72.78$ and $Ro^{-1} \approx 582.22$, respectively. The flow fields for both cases are presented in Fig. 10.

In contrast to the small R case, for larger R, the cold thermal plumes emanating from the inner vertical wall, are thicker and penetrate deeper into the bulk and eventually reach the opposite hot vertical wall. The magnitude of the relative velocities, normalized with the free-fall velocity $\hat{u}_{\text{ff}}$, is smaller for $R = 24$ cm than in the $R = 6$ cm case.

For fixed Ra and Fr, the fluid flow appears to be less turbulent in a physically larger facility, compared to a smaller one. This observation might be considered as counterintuitive, however, it is easy to explain: for the same values of Ra and Fr, the larger R leads to larger values of Ro^{-1}, which in turn means that the turbulent mixing in the vertical direction is more suppressed in the larger Ro^{-1} cases compared to the lower Ro^{-1} cases. The latter follows from the Taylor–Proudman theorem and was observed in plenty experiments and numerical simulations, see, e.g., a review on rotating thermal convection by Ecke and Shishkina [69].

Finally, we present our DNS results for control parameters which are identical to those in one experiment conducted by Jiang et al. [33]. The considered control parameters (in our notations) are $Ra = 8.88 \times 10^8$, $Fr = 6.53$, and $Ro^{-1} = 49.94$ ($R = 24$ cm). From Supplemental material of [33] we extracted details on the fluid properties and container size as well as the Rayleigh number $Ra_{\text{ACRBC}} = 6.58 \times 10^8$ and inverse Rossby number $Ro^{-1}_{\text{ACRBC}} = 58$ (in their notations), which allowed us to calculate the physical values of Δ and Ω in the experiment and finally to calculate Fr, Ra and Ro in our notations. Details regarding the notation transformation from those used in [33,34] to the control parameters we use in the present paper can be found in Appendix A.1.

A snapshot of the instantaneous flow field and the corresponding instantaneous temperature distributions for the case $Ra = 8.88 \times 10^8$, $Fr = 6.53$, and $Ro^{-1} = 49.94$ ($R = 24$ cm) are presented in Fig. 11. Fig. 11(a) shows the global flow structure that exhibits six vertically aligned rolls. The snapshots of the temperature in three horizontal cross-sections, see Fig. 11(b–d), show a three-dimensional flow structure, with fluctuating thermal plumes. Remarkable is that in this turbulent Oberbeck–Boussinesq case, the time- and volume-averaged bulk temperature $\theta_{\text{bulk}} \approx 0.18$ is larger than the mean temperature of the fluid in the pure conduction case, $\theta_c \approx 0.112$. Therefore, to make the presentation of the temperature field clearer, we used the bulk temperature $\theta_{\text{bulk}} \approx 0.18$ as the reference temperature that corresponds to white colour in Fig. 11(b–d).

4.4. Heat and momentum transport

The global heat flux in the CC system is represented by the Nusselt number Nu, which is the ratio of the total heat flux q from the outer heated vertical wall to the inner cooled vertical wall to the corresponding heat flux q_c that would occur via heat conduction alone, in the absence of convection,

$$Nu \equiv q/q_c. \tag{37}$$

From the temperature equation (12) in a general case, it follows that the radial heat flux,[3] averaged in time and in azimuthal and in vertical direction, is constant for any r.

$$q = r(\kappa \partial_r \langle\theta\rangle_{\varphi,z,t} - \langle u_r \theta\rangle_{\varphi,z,t}) = \text{const} \quad \forall r. \tag{38}$$

To calculate q_c in pure conduction case, one can use the temperature equation in cylinder coordinates, Eq. (22), the solution of which is given in Eq. (23). Combining Eq. (23) with Eq. (38) for $\boldsymbol{u} = 0$, we obtain

$$q_c = \frac{\kappa \Delta}{\log(1 - 2\pi/\Gamma_\phi)^{-1}}. \tag{39}$$

Thus, the Nusselt number[4] in a CC system can be calculated for any r, $r \in [R - L, R]$, as follows:

$$Nu \equiv \frac{q}{q_c} = \frac{r(\langle u_r \theta\rangle_{\varphi,z,t} - \kappa \partial_r \langle\theta\rangle_{\varphi,z,t})}{\kappa \Delta \left[\log(1 - 2\pi/\Gamma_\phi)\right]^{-1}}. \tag{40}$$

In addition to the heat transport we also investigate the momentum transport, which is characterized by the Reynolds number[5]

$$Re \equiv \frac{L\, u_{\max}}{\nu}, \tag{41}$$

[3] Formally, the heat flux is in the direction opposite to the radial r-direction, i.e., from the outer annulus wall to the inner wall. However, for simplicity we call it radial heat flux.

[4] From the non-dimensional quantities u_r and θ, the Nusselt number is evaluated as

$$Nu = r \log(1 - 2\pi/\Gamma_\phi) \left(\sqrt{\frac{\Gamma_\phi^3\, Ra\, Pr}{8\pi^3}} \langle u_r \theta\rangle_{\varphi,z,t} - \partial_r \langle\theta\rangle_{\varphi,z,t} \right).$$

[5] From the non-dimensional velocity components, the Reynolds number is evaluated as

$$Re = \sqrt{\frac{\Gamma_\phi}{2\pi} \frac{Ra}{Pr}} \max_r \left\{ \sqrt{\langle u_r^2 + u_\varphi^2 + u_z^2\rangle_{\varphi,z,t}(r)} \right\}.$$

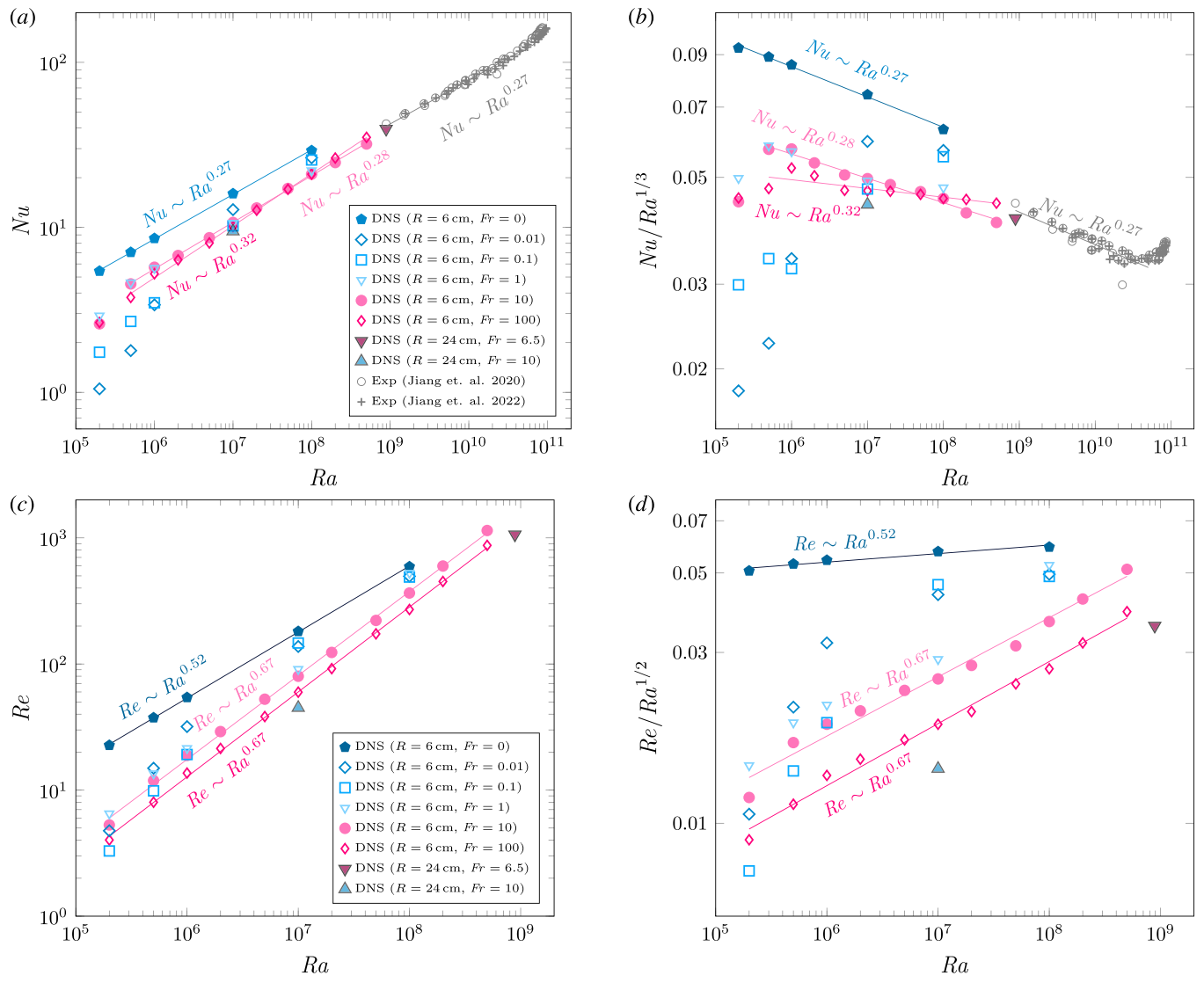

Fig. 12. Transport properties in CC, obtained in our DNS, as functions of the Rayleigh number Ra: (a) the Nusselt number Nu; (b) the Nusselt number compensated by $Ra^{1/3}$; (c) the Reynolds number, based on the maximal over the radial coordinate r kinetic energy, $\max_r\{\sqrt{\langle u_r^2+u_\varphi^2+u_z^2\rangle_{\varphi,z,t}}\}$; (d) the Reynolds number Re normalized by $Ra^{1/2}$. One can clearly see that with increasing Fr, the CC flow undergoes a transition, and in this parameter range, the transport scaling properties of the CC flow are between those for the limiting cases of vertical convection, where $Nu \sim Ra^{1/4}$, $Re \sim Ra^{1/2}$ [22], and Rayleigh–Bénard convection, where $Nu \sim Ra^{1/3}$, $Re \sim Ra^{2/3}$ [15,70,71]. More precisely, the scaling exponents vary from 0.27 to 0.32 in the Nusselt number scaling relation, and from 0.52 to 0.67 in the Reynolds number scaling relation. (For interpretation of the references to colour in this figure legend, the reader is referred to the web version of this article.)

where

$$u_{\max} \equiv \max_r\{\sqrt{\langle u_r^2+u_\varphi^2+u_z^2\rangle_{\varphi,z,t}(r)}\}. \tag{42}$$

The results on the scaling relations for Nu and Re are presented in Fig. 12. There we see, as expected before, that with increasing Fr, the centrifugal convective flow undergoes a transition from the vertical-convection type of the flow to the Rayleigh–Bénard-convection type. The transport scaling properties undergo a transition from those typical for vertical convection, where $Nu \sim Ra^{1/4}$, $Re \sim Ra^{1/2}$, see [22], to those typical for Rayleigh–Bénard convection in the considered parameter range, i.e., $Nu \sim Ra^{1/3}$, $Re \sim Ra^{2/3}$, see [15,70,71].

For large values of Froude number ($Fr \gg 1$) we expect a transition to the ultimate regime [11,27,32], with an increased exponent (>1/3) in the Nu versus Ra scaling relation, as soon as the Rayleigh number achieves sufficiently large values. However, in our DNS, the values of the considered Ra are not large enough to observe this transition.

As discussed above, for fixed Ra and Fr, the fluid flow is less turbulent in a physically larger facility, compared to a smaller one. This is also reflected in the Nusselt numbers and Reynolds numbers. Thus for the same $Ra = 10^7$ and $Fr = 10$, but different radii, $R = 6$ cm and $R = 24$ cm, which correspond to different inverse Rossby numbers, $Ro^{-1} \approx 72.78$ and $Ro^{-1} \approx 582.22$, respectively, we obtained different Nusselt numbers: $Nu \approx 10.7$ and $Re \approx 80$ for the $R = 6$ cm container and $Nu \approx 9.5$ and $Re \approx 45$ for the $R = 24$ cm container.

Finally, we mention our DNS results on the transport properties for the case, which was also studied experimentally in the ACRBC facility [33], namely for $Ra = 8.88 \times 10^8$, $Fr = 6.53$, and $Ro^{-1} = 49.94$ ($R = 24$ cm).[6] This case is marked with a pink filled triangle in Figs. 2,

[6] In the notations used in Jiang et al. [33,34], this case is equivalent to $Ra_{\mathrm{ACRBC}} = 6.58 \times 10^8$, $Fr_{\mathrm{ACRBC}} \equiv a_c/g = 4.9$, and $Ro^{-1} = 58.0$ ($R = 24$ cm). See Appendix A.1 for the notation transformation.

9 and 12. The Nusselt number obtained in our DNS, $Nu = 39.40$, is 7% smaller than experimentally measured Nusselt number [33] for this case, $Nu_{\mathrm{ACRBC}} = 42.45$.

5. Summary

Centrifugal convection (CC) is a prosperous system that, in particular, allows the investigation of the regime of high Rayleigh numbers in thermal convection of Rayleigh–Bénard type, by increasing the rotation rate (i.e., by increasing the centrifugal acceleration). In addition, for any rotation rates, the system experiences gravitational acceleration, which provides additional shear to the system and thus eases a transition to the ultimate regime by relatively low Rayleigh numbers.

In the present study, for the Rayleigh numbers up to 8.88×10^8 and Froude numbers from 0 to 100, we have investigated the transition from the gravitational buoyancy dominance (when the flow properties are similar to those in vertical convection) to the centrifugal buoyancy dominance (when the system is similar to Rayleigh–Bérnard system, "lying on a side"). This transition is indeed seen in the changing global flow structure and in the scaling relations for the Nusselt number and Reynolds number versus the Rayleigh number.

The differences between CC and classical Rayleigh–Bérnard convection include the presence of an additional shear in the system due to the unavoidable presence of gravitational buoyancy in the direction orthogonal to the centrifugal buoyancy. Another difference is that for any rotation rate ($Fr \neq 0$), the driving centrifugal acceleration depends on the radial distance, which becomes very relevant for not that large values of Γ_ϕ, while in the classical Rayleigh–Bénard setup, the driving gravitational acceleration is constant. Finally, the curved geometry of the container also influences the CC flow, in particular, it leads to an increased bulk temperature which is always larger than the arithmetic mean of the temperatures of the heated and cooled vertical walls.

We anticipate many further exciting experimental and numerical studies on CC systems to come, in particular those aimed at the investigation of the ultimate regime by extremely large Rayleigh numbers and transition to this regime. As said, compared to the classical Rayleigh–Bénard convection, CC favours the earlier transition to the ultimate regime due to the additional shear, which makes this system of particular interest.

CRediT authorship contribution statement

Zhongzhi Yao: Writing – review & editing, Visualization, Validation, Formal analysis. **Mohammad S. Emran:** Writing – review & editing, Validation, Software, Investigation, Formal analysis, Data curation. **Andrei Teimurazov:** Writing – review & editing, Visualization, Validation, Supervision, Software, Investigation, Formal analysis, Data curation. **Olga Shishkina:** Writing – review & editing, Writing – original draft, Validation, Supervision, Software, Resources, Project administration, Methodology, Investigation, Funding acquisition, Conceptualization.

Declaration of competing interest

The authors declare that they have no known competing financial interests or personal relationships that could have appeared to influence the work reported in this paper.

Acknowledgements

The authors would like to acknowledge the valuable discussions and insights provided by Chao Sun, Jiaxing Song, Detlef Lohse and Eberhard Bodenschatz. The authors acknowledge the financial support from the Deutsche Forschungsgemeinschaft, Germany under the grants Sh405/20 and Sh405/22, the China Scholarship Council (CSC) under grant No. 202208460009 and the Max Planck Computing and Data Facility (MPCDF), Germany in Munich.

Appendix

A.1. Notation transformation

In this subsection we will show how one can calculate the values of the control parameters Ra, Fr and Ro using quantities introduced in the experimental study by Jiang et al. [33,34]. The Rayleigh number for the ACRBC facility [33,34] was defined as

$$Ra_{\mathrm{ACRBC}} \equiv \frac{\alpha \Omega^2 (R - L/2) L^3 \Delta}{\kappa \nu} \tag{A.1}$$

and the Rossby number as

$$Ro_{\mathrm{ACRBC}} \equiv \sqrt{\alpha \Delta \left(\frac{\Gamma_\phi}{8\pi} - \frac{1}{8} \right)}. \tag{A.2}$$

The Froude number was not introduced in the main text of the papers [33,34]. However, in the main table of the Supplemental materials of [34], one can find the quantity of the centrifugal acceleration over gravitational acceleration, called "a_c/g", which we call here as the Froude number for the ACRBC facility:

$$Fr_{\mathrm{ACRBC}} \equiv \frac{\Omega^2 (R - L/2)}{g_z}. \tag{A.3}$$

Combining Eqs. (A.1), (A.2) and (A.3), to obtain the control parameters from Eqs. (5), (7) and (8), we derive the following:

$$Ra = Ra_{\mathrm{ACRBC}} \left(\left(1 - \pi/\Gamma_\phi\right)^{-2} + Fr_{\mathrm{ACRBC}}^{-2} \right)^{1/2}, \tag{A.4}$$

$$Ro = Ro_{\mathrm{ACRBC}} \left(\left(1 - \pi/\Gamma_\phi\right)^{-2} + Fr_{\mathrm{ACRBC}}^{-2} \right)^{1/4}, \tag{A.5}$$

and

$$Fr = \frac{Fr_{\mathrm{ACRBC}}}{1 - \pi/\Gamma_\phi}. \tag{A.6}$$

When $Fr_{\mathrm{ACRBC}} \to \infty$, then $Fr \to \infty$ as well, and Eqs. (A.4) and (A.5) are reduced to

$$Ra \to \frac{Ra_{\mathrm{ACRBC}}}{1 - \pi/\Gamma_\phi}, \tag{A.7}$$

$$Ro \to \frac{Ro_{\mathrm{ACRBC}}}{\sqrt{1 - \pi/\Gamma_\phi}}. \tag{A.8}$$

In our simulations and in the experiments by Jiang et al. [33,34], $\Gamma_\phi = 4\pi$ and therefore in the case $Fr_{\mathrm{ACRBC}} \to \infty$, Eqs. (A.4), (A.5) and (A.6) are further reduced to

$$Ra \to \frac{4}{3} Ra_{\mathrm{ACRBC}}, \tag{A.9}$$

$$Ro \to \frac{2}{\sqrt{3}} Ro_{\mathrm{ACRBC}}, \tag{A.10}$$

and

$$Fr \to \infty. \tag{A.11}$$

However, in most of our simulations, the Froude number is not that large, therefore, we need to know all of the four parameters of the system, Ra, Fr, Ro, Pr (in addition to the geometrical aspect ratios Γ_ϕ and Γ_H), and a link to the experimental data of Jiang et al. [33,34] is provided through the formulas in Eqs. (A.4), (A.5) and (A.6).

A.2. Details on the direct numerical simulations

In the following table we report all relevant control parameters and responses of the CC system studied in our DNS.

Data availability

Data will be made available on request.

Table A.1
Details on the conducted direct numerical simulations: Rayleigh number Ra, Eq. (5); Froude number Fr, Eq. (8); inverse Rossby number Eq. (7); grid resolution $N_\phi \times N_r \times N_z$, where N_φ, N_r, and N_z are the number of nodes in the φ-, r-, and z-directions, respectively; the time- and volume averaged Nusselt number Nu, Eq. (40); the standard deviation of the Nusselt number $\sigma_{Nu} \equiv \left(\frac{1}{N} \sum_{n=1}^{N} \left(Nu_n - Nu \right)^2 \right)^{1/2}$, where Nu_n is the Nusselt number at a time slice n, and N is the total number of the slices used for statistical averaging; time of statistical averaging t_{avg} measured in the free-fall time units; normalized time- and volume-averaged temperature of the fluid (with subtracted arithmetic mean of the temperatures of the heated and cooled vertical surfaces) $\theta_{\text{bulk}}/\Delta$; Reynolds number Re based on the averaged in time and in the ϕ- and z-directions maximal over r kinetic energy, Eqs. (41) and (42); and the ratio of the maximal in the r-direction grid stepping h to the Batchelor microscale η_B, Eq. (21). In all DNS, the Prandtl number is set to $Pr = 4.3$. In almost all cases, the outer radius of the container is taken $R = 6$ cm, except for the last two simulations marked with symbol †, where $R = 24$ cm, as in the experiments by Jiang et al. [33,34]. Since the fluid parameters and the shape and size of the container are fixed, the system has only two independent parameters, which are Ra and Fr, while the Rossby number Ro is a dependent characteristic which can be calculated via Eq. (8). Note that the accuracy of the calculations of the Nusselt number Nu is assessed with the quantity $\left(\frac{1}{N_r} \sum_{r=1}^{N_r} \left(\langle Nu(t,r,\phi,z) \rangle_{t,\phi,z} - Nu \right)^2 \right)^{1/2}$, which is smaller than 0.02 for all studied cases. Dash symbols in the σ_{Nu} and t_{avg} columns mean that the flows are steady. Note further that in all studied cases the bulk temperature θ_{bulk} is larger than the arithmetic mean (which is equal to zero) of the temperatures of the heated and cooled vertical surfaces of the container, while the bulk temperature in the pure conduction case equals $\theta_c \approx 0.112$. Final note is that the grid spacing h is compared to the Batchelor microscale η_B and not to the Kolmogorov microscale, since the latter quantity is $\sqrt{Pr}$ times larger than η_B.

Ra	Fr	Ro^{-1}	$N_\phi \times N_r \times N_z$	Nu	σ_{Nu}	t_{avg}	$\theta_{\text{bulk}}/\Delta$	Re	h/η_B
2×10^5	0	0	$512 \times 128 \times 128$	5.43	–	–	0.141	22.67	0.27
2×10^5	0.01	16.27	$512 \times 128 \times 128$	1.05	–	–	0.110	4.76	0.18
2×10^5	0.1	51.46	$512 \times 128 \times 128$	1.75	–	–	0.115	3.29	0.17
2×10^5	1	162.73	$512 \times 128 \times 128$	2.91	–	–	0.145	6.50	0.27
2×10^5	10	514.61	$512 \times 128 \times 128$	2.60	–	–	0.145	5.29	0.29
2×10^5	100	1627.35	$512 \times 128 \times 128$	2.65	–	–	0.123	4.02	0.28
5×10^5	0	0	$512 \times 128 \times 128$	7.06	–	–	0.145	37.49	0.40
5×10^5	0.01	10.29	$512 \times 128 \times 128$	1.79	–	–	0.103	14.91	0.30
5×10^5	0.1	32.55	$512 \times 128 \times 128$	2.69	–	–	0.121	9.87	0.27
5×10^5	1	102.92	$512 \times 128 \times 128$	4.62	–	–	0.132	13.52	0.40
5×10^5	10	325.47	$512 \times 128 \times 128$	4.54	–	–	0.129	11.90	0.44
5×10^5	100	1029.22	$512 \times 128 \times 128$	3.75	–	–	0.138	8.01	0.40
10^6	0	0	$512 \times 128 \times 128$	8.57	–	–	0.148	54.29	0.50
10^6	0.01	7.28	$512 \times 128 \times 128$	3.39	–	–	0.103	31.87	0.42
10^6	0.1	23.01	$512 \times 128 \times 128$	3.23	–	–	0.129	19.14	0.38
10^6	0.5	51.46	$512 \times 128 \times 128$	5.15	–	–	0.128	17.49	0.44
10^6	1	72.78	$512 \times 128 \times 128$	5.66	–	–	0.129	21.42	0.50
10^6	2	102.92	$512 \times 128 \times 128$	5.87	–	–	0.130	22.64	0.54
10^6	3	126.05	$512 \times 128 \times 128$	5.89	–	–	0.130	22.16	0.55
10^6	4	145.55	$512 \times 128 \times 128$	5.87	–	–	0.129	21.52	0.56
10^6	5	162.73	$512 \times 128 \times 128$	5.85	–	–	0.129	20.93	0.56
10^6	7	192.55	$512 \times 128 \times 128$	5.80	–	–	0.129	19.94	0.56
10^6	10	230.14	$512 \times 128 \times 128$	5.73	–	–	0.128	18.85	0.55
10^6	20	325.47	$512 \times 128 \times 128$	5.58	–	–	0.128	16.81	0.55
10^6	30	398.62	$512 \times 128 \times 128$	5.48	–	–	0.128	15.77	0.54
10^6	40	460.28	$512 \times 128 \times 128$	5.41	–	–	0.128	15.13	0.54
10^6	50	514.61	$512 \times 128 \times 128$	5.36	–	–	0.128	14.69	0.53
10^6	70	608.89	$512 \times 128 \times 128$	5.29	–	–	0.128	14.12	0.53
10^6	100	727.77	$512 \times 128 \times 128$	5.23	–	–	0.129	13.64	0.53
2×10^6	10	162.73	$512 \times 128 \times 128$	6.75	–	–	0.134	29.10	0.68
2×10^6	100	514.61	$512 \times 128 \times 128$	6.35	–	–	0.130	21.39	0.66
5×10^6	10	102.92	$768 \times 192 \times 192$	8.64	0.55	1360	0.172	52.57	0.68
5×10^6	100	325.47	$768 \times 192 \times 192$	8.03	0.38	1000	0.172	38.30	0.69
10^7	0	0	$768 \times 192 \times 192$	16.00	–	–	0.157	181.37	0.76
10^7	0.01	2.30	$768 \times 192 \times 192$	12.80	–	–	0.140	137.62	0.64
10^7	0.1	7.28	$768 \times 192 \times 192$	10.23	0.43	1700	0.129	146.64	0.67
10^7	0.4	14.55	$768 \times 192 \times 192$	10.01	0.80	1200	0.149	122.68	0.72
10^7	1	23.01	$768 \times 192 \times 192$	10.75	0.89	1700	0.160	90.89	0.76
10^7	2	32.54	$768 \times 192 \times 192$	10.75	0.84	1400	0.170	91.13	0.79
10^7	5	51.46	$768 \times 192 \times 192$	10.70	0.78	1700	0.177	85.60	0.83
10^7	10	72.78	$768 \times 192 \times 192$	10.67	0.84	1500	0.176	79.93	0.85
10^7	20	102.92	$768 \times 192 \times 192$	10.53	0.69	1400	0.177	73.55	0.85
10^7	50	162.73	$768 \times 192 \times 192$	10.34	0.62	1500	0.176	65.98	0.86
10^7	100	230.14	$768 \times 192 \times 192$	10.16	0.59	1500	0.176	59.78	0.87
2×10^7	10	51.46	$768 \times 192 \times 192$	13.11	1.02	2300	0.178	123.49	1.05
2×10^7	100	162.735	$768 \times 192 \times 192$	12.69	0.90	1350	0.180	91.83	1.08
5×10^7	10	32.54	$1024 \times 256 \times 256$	17.15	1.44	1300	0.176	221.5	1.00
5×10^7	100	102.92	$1024 \times 256 \times 256$	17.00	1.29	1100	0.180	173.3	1.12
10^8	0	0	$1024 \times 256 \times 256$	29.24	–	–	0.163	591.39	1.20
10^8	0.01	0.73	$1024 \times 256 \times 256$	26.41	–	–	0.159	496.40	1.10
10^8	0.1	2.30	$1024 \times 256 \times 256$	25.62	0.01	1500	0.150	488.99	1.06
10^8	0.5	5.14	$1024 \times 256 \times 256$	23.80	0.97	1700	0.150	536.08	1.10
10^8	1	7.28	$1024 \times 256 \times 256$	22.04	1.91	1500	0.155	526.31	1.17
10^8	5	16.27	$1024 \times 256 \times 256$	19.91	1.69	1600	0.170	404.89	1.22
10^8	10	23.01	$1024 \times 256 \times 256$	20.95	1.53	1700	0.174	365.54	1.25
10^8	20	32.55	$1024 \times 256 \times 256$	21.11	1.68	1550	0.178	333.10	1.30
10^8	50	51.46	$1024 \times 256 \times 256$	21.11	1.83	1470	0.181	293.55	1.36
10^8	100	72.78	$1024 \times 256 \times 256$	21.03	1.74	1800	0.183	270.44	1.40
2×10^8	10	16.27	$1024 \times 256 \times 256$	24.67	1.70	2200	0.180	598.28	1.60
2×10^8	100	51.46	$1024 \times 256 \times 256$	26.32	1.87	980	0.189	451.04	1.76

(*continued on next page*)

Table A.1 (*continued*).

5×10^8	10	10.29	$1024\times256\times256$	32.00	2.90	1650	0.200	1144.49	2.12
5×10^8	100	32.54	$1024\times256\times256$	35.03	2.32	1650	0.206	872.22	2.40
10^7 †	10.0	582.22	$768\times192\times192$	9.46	0.64	1300	0.169	44.94	0.83
8.88×10^8 †	6.53	49.94	$1840\times460\times460$	39.40	2.66	1200	0.180	1062.12	1.76

References

[1] C. Clarke, B. Carswell, Principles of Astrophysical Fluid Dynamics, Cambridge University Press, Cambridge, 2007.
[2] B. Cushman-Roisin, J.-M. Beckers, Introduction to Geophysical Fluid Dynamics, second ed., in: Internation Geophysics Series, vol. 101, Elsevier, 2011.
[3] G.K. Vallis, Atmospheric and Oceanic Fluid Dynamics, Cambridge University Press, Cambridge, 2017.
[4] H. Bénard, Les tourbillons cellulairs dans une nappe liquide, Rev. Gén. Sci. Pure Appl. 11 (1900) 1261–1271, 1309–1328.
[5] Lord Rayleigh, On convection currents in a horizontal layer of fluid, when the higher temperature is on the under side, Phil. Mag. 32 (1916) 529–546.
[6] E. Bodenschatz, W. Pesch, G. Ahlers, Recent developments in Rayleigh–Bénard convection, Annu. Rev. Fluid Mech. 32 (2000) 709–778.
[7] G. Ahlers, S. Grossmann, D. Lohse, Heat transfer and large scale dynamics in turbulent Rayleigh–Bénard convection, Rev. Modern Phys. 81 (2009) 503–537.
[8] D. Lohse, K.-Q. Xia, Small-scale properties of turbulent Rayleigh–Bénard convection, Annu. Rev. Fluid Mech. 42 (2010) 335–364.
[9] F. Chillà, J. Schumacher, New perspectives in turbulent Rayleigh–Bénard convection, Eur. Phys. J. E 35 (2012) 58.
[10] O. Shishkina, Rayleigh–Bénard convection: The container shape matters, Phys. Rev. Fluids 6 (2021) 090502.
[11] D. Lohse, O. Shishkina, Ultimate turbulent thermal convection, Phys. Today 76 (2023) 26–32.
[12] G.O. Hughes, R.W. Griffiths, Horizontal convection, Annu. Rev. Fluid Mech. 40 (2008) 185–208.
[13] O. Shishkina, S. Wagner, Prandtl-number dependence of heat transport in laminar horizontal convection, Phys. Rev. Lett. 116 (2016) 024302.
[14] O. Shishkina, S. Grossmann, D. Lohse, Heat and momentum transport scalings in horizontal convection, Geophys. Res. Lett. 43 (2016) 1219–1225.
[15] O. Shishkina, M.S. Emran, S. Grossmann, D. Lohse, Scaling relations in large-prandtl-number natural thermal convection, Phys. Rev. Fluids 2 (2017) 103502.
[16] T. Tsai, W.K. Hussam, M.P. King, G.J. Sheard, Transitions and scaling in horizontal convection driven by different temperature profiles, Int. J. Therm. Sci. 148 (2020) 106166.
[17] P. Reiter, O. Shishkina, Classical and symmetrical horizontal convection: Detaching plumes and oscillations, J. Fluid Mech. 892 (2020) R1.
[18] S.-S. Ding, K.L. Chong, J.-Q. Shi, G.-Y. Ding, H.-Y. Lu, K.-Q. Xia, J.-Q. Zhong, Inverse centrifugal effect induced by collective motion of vortices in rotating thermal convection, Nature Commun. 12 (2021) 5585.
[19] B. Yan, O. Shishkina, X. He, Thermal boundary-layer structure in laminar horizontal convection, J. Fluid Mech. 915 (2021) R5.
[20] A. Belmonte, A. Tilgner, A. Libchaber, Turbulence and internal waves in side-heated convection, Phys. Rev. E 51 (1995) 5681–5687.
[21] H. Yu, N. Li, R.E. Ecke, Scaling in laminar natural convection in laterally heated cavities: Is turbulence essential in the classical scaling of heat transfer? Phys. Rev. E 76 (2007) 026303.
[22] O. Shishkina, Momentum and heat transport scalings in laminar vertical convection, Phys. Rev. E 93 (2016) 051102(R).
[23] C.S. Ng, A. Ooi, D. Lohse, D. Chung, Vertical natural convection: Application of the unifying theory of thermal convection, J. Fluid Mech. 764 (2015) 0349–361.
[24] C.S. Ng, A. Ooi, D. Lohse, D. Chung, Changes in the boundary-layer structure at the edge of the ultimate regime in vertical natural convection, J. Fluid Mech. 825 (2017) 550–572.
[25] Q. Wang, D. Lohse, O. Shishkina, Scaling in internally heated convection: a unifying theory, Geophys. Res. Lett. 48 (2021) e2020GL091198.
[26] L. Zwirner, M. Emran, F. Schindler, S. Singh, S. Eckert, T. Vogt, O. Shishkina, Dynamics and length scales in vertical convection of liquid metals, J. Fluid Mech. 932 (2022) A9.
[27] D. Lohse, O. Shishkina, Ultimate Rayleigh–Bénard turbulence, Rev. Modern Phys. 96 (2024) 035001.
[28] G. Ahlers, X. He, D. Funfschilling, E. Bodenschatz, Heat transport by turbulent Rayleigh–Bénard convection for $Pr\sim0.8$ and $3\times10^{12}\lesssim Ra\lesssim10^{15}$: Aspect ratio $\Gamma=0.50$, New J. Phys. 14 (2012) 103012.
[29] X. He, D. Funfschilling, H. Nobach, E. Bodenschatz, G. Ahlers, Transition to the ultimate state of turbulent Rayleigh–Bénard convection, Phys. Rev. Lett. 108 (2012) 024502.
[30] X. He, D. Funfschilling, E. Bodenschatz, G. Ahlers, Heat transport by turbulent Rayleigh–Bénard convection for $Pr\sim0.8$ and $4\times10^{11}\lesssim Ra\lesssim2\times10^{14}$: Ultimate-state transition for aspect ratio $\Gamma=1.00$, New J. Phys. 14 (2012) 063030.
[31] P.-E. Roche, F. Gauthier, R. Kaiser, J. Salort, On the triggering of the ultimate regime of convection, New J. Phys. 12 (2010) 085014.
[32] P.-E. Roche, The ultimate state of convection: a unifying picture of very high Rayleigh numbers experiments, New J. Phys. 22 (2020) 073056.
[33] H. Jiang, X. Zhu, D. Wang, S.G. Huisman, C. Sun, Supergravitational turbulent thermal convection, Sci. Adv. 6 (2020) eabb8676.
[34] H. Jiang, D. Wang, S. Liu, C. Sun, Experimental evidence for the existence of the ultimate regime in rapidly rotating turbulent thermal convection, Phys. Rev. Lett. 129 (2022) 204502.
[35] K.E. Daniels, R.J. Wiener, E. Bodenschatz, Localized transverse bursts in inclined layer convection, Phys. Rev. Lett. 91 (2003) 114501.
[36] F. Chillà, M. Rastello, S. Chaumat, B. Castaing, Long relaxation times and tilt sensitivity in Rayleigh–Bénard turbulence, Eur. Phys. J. B 40 (2004) 223–227.
[37] C. Sun, H.-D. Xi, K.-Q. Xia, Azimuthal symmetry, flow dynamics, and heat transport in turbulent thermal convection in a cylinder with an aspect ratio of 0.5, Phys. Rev. Lett. 95 (2005) 074502.
[38] G. Ahlers, E. Brown, A. Nikolaenko, The search for slow transients, and the effect of imperfect vertical alignment, in turbulent Rayleigh–Bénard convection, J. Fluid Mech. 557 (2006) 347–367.
[39] X. Riedinger, J.-C. Tisserand, F. Seychelles, B. Castaing, F. Chillá, Heat transport regimes in an inclined channel, Phys. Fluids 25 (2013) 015117.
[40] S. Weiss, G. Ahlers, Effect of tilting on turbulent convection: cylindrical samples with aspect ratio γ=0.50, J. Fluid Mech. 715 (2013) 314–334.
[41] R. Langebach, C. Haberstroh, Natural convection in inclined pipes - A new correlation for heat transfer estimations, in: J.G. Weisend, et al. (Eds.), Advances in Cryogenic Engineering, in: AIP Conf. Proc., vol. 1573, 2014, pp. 1504–1511.
[42] P. Frick, R. Khalilov, I. Kolesnichenko, A. Mamykin, V. Pakholkov, A. Pavlinov, S.A. Rogozhkin, Turbulent convective heat transfer in a long cylinder with liquid sodium, Europhys. Lett. 109 (2015) 14002.
[43] A. Mamykin, P. Frick, R. Khalilov, I. Kolesnichenko, V. Pakholkov, S. Rogozhkin, A. Vasiliev, Turbulent convective heat transfer in an inclined tube with liquid sodium, Magnetohydrodynamics 51 (2015) 329–336.
[44] A.Y. Vasil'ev, I.V. Kolesnichenko, A.D. Mamykin, P.G. Frick, R.I. Khalilov, S.A. Rogozhkin, V.V. Pakholkov, Turbulent convective heat transfer in an inclined tube filled with sodium, Tech. Phys. 60 (2015) 1305–1309.
[45] I. Kolesnichenko, A.D. Mamykin, A.M. Pavlinov, V.V. Pakholkov, S.A. Rogozhkin, P.G. Frick, R.I. Khalilov, S.F. Shepelev, Experimental study on free convection of sodium in a long cylinder, Therm. Eng. 62 (2015) 414–422.
[46] R. Khalilov, I. Kolesnichenko, A. Pavlinov, A. Mamykin, A. Shestakov, P. Frick, Thermal convection of liquid sodium in inclined cylinders, Phys. Rev. Fluids 3 (2018) 043503.
[47] O. Shishkina, S. Horn, Thermal convection in inclined cylindrical containers, J. Fluid Mech. 790 (2016) R3.
[48] A. Teimurazov, P. Frick, Thermal convection of liquid metal in a long inclined cylinder, Phys. Rev. Fluids 2 (2017) 113501.
[49] L. Zwirner, O. Shishkina, Confined inclined thermal convection in low-Prandtl-number fluids, J. Fluid Mech. 850 (2018) 984–1008.
[50] S.D. Mandrykin, A.S. Teimurazov, Turbulent convection of liquid sodium in an inclined cylinder of unit aspect ratio, J. Appl. Mech. Tech. Phys. 60 (2019) 1237–1248.
[51] L. Zwirner, A. Tilgner, O. Shishkina, Elliptical instability and multiple-roll flow modes of the large-scale circulation in confined turbulent Rayleigh–Bénard convection, Phys. Rev. Lett. 125 (2020) 054502.
[52] V.D. Zimin, P.G. Frik, V.G. Shaidurov, Turbulent convection in a cubic cell heated simultaneously on the side and the bottom, Fluid Dyn. 17 (1982) 286–290.
[53] A. Fabregat, J. Pallares, Heat transfer and boundary layer analyses of laminar and turbulent natural convection in a cubical cavity with differently heated opposed walls, Int. J. Heat Mass Transfer 151 (2020) 119409.
[54] A. Teimurazov, P. Reiter, O. Shishkina, P. Frick, Heat transport in a cell heated at the bottom and the side, Europhys. Lett. 134 (2021) 34001.
[55] O. Shishkina, S. Horn, S. Wagner, E.S.C. Ching, Thermal boundary layer equation for turbulent Rayleigh–Bénard convection, Phys. Rev. Lett. 114 (2015) 114302.
[56] G.L. Kooij, M.A. Botchev, E.M. Frederix, B.J. Geurts, S. Horn, D. Lohse, E.P. van der Poel, O. Shishkina, R.J.A.M. Stevens, R. Verzicco, Comparison of computational codes for direct numerical simulations of turbulent Rayleigh–Bénard convection, Comput. & Fluids 166 (2018) 1–8.
[57] P. Reiter, X. Zhang, R. Stepanov, O. Shishkina, Generation of zonal flows in convective systems by travelling thermal waves, J. Fluid Mech. 913 (2021) A13.
[58] P. Reiter, X. Zhang, O. Shishkina, Flow states and heat transport in Rayleigh–Bénard convection with different sidewall boundary conditions, J. Fluid Mech. 936 (2022) A32.
[59] M.S. Emran, O. Shishkina, Natural convection in cylindrical containers with isothermal ring-shaped obstacles, J. Fluid Mech. 882 (2020) A3.

[60] S. Horn, O. Shishkina, Rotating non-Oberbeck–Boussinesq Rayleigh–Bénard convection in water, Phys. Fluids 26 (2014) 055111.
[61] S. Horn, O. Shishkina, Toroidal and poloidal energy in rotating Rayleigh–Bénard convection, J. Fluid Mech. 762 (2015) 232–255.
[62] X. Zhang, D.P.M. van Gils, S. Horn, M. Wedi, L. Zwirner, G. Ahlers, R.E. Ecke, S. Weiss, E. Bodenschatz, O. Shishkina, Boundary zonal flow in rotating turbulent Rayleigh–Bénard convection, Phys. Rev. Lett. 124 (2020) 084505.
[63] X. Zhang, R.E. Ecke, O. Shishkina, Boundary zonal flows in rapidly rotating turbulent thermal convection, J. Fluid Mech. 915 (2021) A62.
[64] R.E. Ecke, X. Zhang, O. Shishkina, Connecting wall modes and boundary zonal flows in rotating Rayleigh–Bénard convection, Phys. Rev. Fluids 7 (2022) L011501.
[65] X. Zhang, P. Reiter, O. Shishkina, R.E. Ecke, Wall modes and the transition to bulk convection in rotating Rayleigh–Bénard convection, Phys. Rev. Fluids 9 (2024) 053501.
[66] O. Shishkina, R.J.A.M. Stevens, S. Grossmann, D. Lohse, Boundary layer structure in turbulent thermal convection and its consequences for the required numerical resolution, New J. Phys. 12 (2010) 075022.
[67] D. Wang, H. Jiang, S. Liu, X. Zhu, C. Sun, Effects of radius ratio on annular centrifugal Rayleigh–Bénard convection, J. Fluid Mech. 930 (2022) A19.
[68] X.Z. Wu, A. Libchaber, Non-Boussinesq effects in free thermal convection, Phys. Rev. A 43 (1991) 2833–2839.
[69] R.E. Ecke, O. Shishkina, Turbulent rotating Rayleigh–Bénard convection, Annu. Rev. Fluid Mech. 55 (2023) 603–638.
[70] S. Grossmann, D. Lohse, Scaling in thermal convection: A unifying theory, J. Fluid Mech. 407 (2000) 27–56.
[71] S. Grossmann, D. Lohse, Thermal convection for large Prandtl numbers, Phys. Rev. Lett. 86 (2001) 3316–3319.